International Journal of Multiphase Flow 191 (2025) 105307

Contents lists available at ScienceDirect

International Journal of Multiphase Flow

journal homepage: www.elsevier.com/locate/ijmulflow

Research Paper

Capillary trapping in mixed-wet porous media: Implications for subsurface carbon dioxide sequestration

Saideep Pavuluri [a,*], Thomas Daniel Seers [a], Nima Shokri [b,c], Nayef Alyafei [d], Harris Sajjad Rabbani [a,e,**]

[a] Department of Petroleum Engineering, Texas A&M University at Qatar, Education City, Doha, 23874, Qatar
[b] Institute of Geo-Hydroinformatics, Hamburg University of Technology, Hamburg, Germany
[c] United Nations University Hub on Engineering to Face Climate Change at the Hamburg University of Technology, United Nations University Institute for Water, Environment and Health (UNU-INWEH), Hamburg, Germany
[d] Department of Chemical Engineering, Qatar University, Doha, Qatar
[e] College of Science and Engineering, Hamad Bin Khalifa University, Education City, Doha, 34110, Qatar

ARTICLE INFO

Keywords:
Mixed-wet porous media
Multiphase flows
Direct numerical simulations
Viscous fingering
Capillary trapping

ABSTRACT

Subsurface sequestration of carbon dioxide (CO_2) is driving efforts to attain carbon neutrality. For the safe and optimal operation of such complex applications, it is imperative to understand the physics of fluids displacement. Direct numerical simulations are used to investigate the flooding of two immiscible fluids having viscosity contrasts in mixed-wet porous media, which are ubiquitous in reservoirs characterized by multifarious mineralogizes and complex physico-chemical histories. Three mixed-wet systems having different wettability ranges and one mono-wet case are considered for investigation. Flooding by low viscosity fluid caused fingering. Though the fingering patterns vary for different wettability distributions, the sample-scale morphological metrics for all cases are closely comparable. The fingering profiles are preserved and later subjected to flooding by high viscosity fluid. Entrapment of the defending phase due to capillarity for different wettability systems are investigated. When the wettability range increases, the trapping efficiency is also seen to increase linearly, suggesting that reservoirs with strong mixed-wet conditions present an attractive option for CO_2 sequestration. Pore-scale fluid displacements reveal that during viscous fingering the fluid-fluid interface initially developed in non-wet zones retract which contribute towards cooperative pore filling in the surrounding wetting zones that influence the characteristic features of invading fluid's flow morphology. Additionally, various possibilities by which the defending phase gets trapped by flow bypassing are explored. Trapping was prominent in zones having an affinity to the defending phase. The average trapped ganglia size increases commensurately with degree of dispersion in wettability. The study also highlights shortcomings of analyzing multiphase flows in mono-wet systems. Insights from this study can be used for improving pore network models and training machine learning algorithms.

1. Introduction

In the drive towards net zero emissions, the field-scale sequestration of carbon dioxide (CO_2) within subsurface formations is being actively explored and implemented. Geologic porous media targeted for carbon capture and storage (CCS) exhibit pronounced variability in rock physical properties which fundamentally modulate the transport behavior of the injected CO_2. Indeed, the degree to which such behaviors can be encapsulated numerically and modeled has a major bearing upon our ability to safely and economically execute carbon sequestration projects, which represent one of the defining geo-engineering challenges of our time. To optimize and strategize the performance of CCS applications, experimental and numerical studies that emulate reservoir conditions have served as valuable tools to study the overarching flow physics operating within potential storage formations (Jiang, 2011; Liu et al., 2012; Lei et al., 2015; Fernø et al., 2024; Flemisch et al., 2024). Among the CO_2 trapping mechanisms identified by such studies that include capillary, structural, solubility and mineral trapping, capillary trapping - in which the defending phase (CO_2) is immobilized in the

* Corresponding author.
** Corresponding author at: College of Science and Engineering, Hamad Bin Khalifa University, Education City, Doha, 34110, Qatar.
E-mail addresses: spavuluri@hbku.edu.qa (S. Pavuluri), thomas.seers@qatar.tamu.edu (T. Daniel Seers), nima.shokri@tuhh.de (N. Shokri), N.alyafei@qu.edu.qa (N. Alyafei), hrabbani@hbku.edu.qa (H. Sajjad Rabbani).

https://doi.org/10.1016/j.ijmultiphaseflow.2025.105307
Received 2 February 2025; Received in revised form 22 May 2025; Accepted 26 May 2025
Available online 20 June 2025

pore space due to capillary effects, is considered to be of primary importance. The entrapment of CO_2 by capillary trapping occurs due to (i). flow bypassing and/or (ii). snap-off mechanisms (Chatzis et al., 1983; Hu et al., 2017). During flow bypassing, the invading fluid preferentially flows through specific flow paths, with invasion curbed within certain regions of the porous medium due to high capillary entry pressures. This eventually results in trapping of the defending phase in those pore spaces that remain uninvaded. Conversely, during snap-off, the wetting films on the surfaces of pore constrictions (i.e., throats) swell until they eventually merge and trap the non-wetting fluid in the adjacent pore body connected to the throat. Zhang and Arif (2024) provide a comprehensive discussion regarding parameters that influence capillary trapping, including petrophysical properties (porosity, permeability), physico-chemical properties (wettability, surface tension) and operational conditions (flow rates, thermodynamic setting).

Wettability describes the affinity of a given fluid with a solid surface in the presence of another immiscible fluid, quantified by the contact angle θ (Morrow, 1990). Many intriguing pore-scale insights related to dynamic flow behavior have been identified while studying the role of wettability in complex pore geometries (Ferrari and Lunati, 2013; Rabbani et al., 2016, 2018; Rabbani and Seers, 2019; Pavuluri et al., 2020, 2023) which consequently impacts the flow morphology at larger scales. In the context of CCS, though it is evident from previous studies that wettability impacts the capillary trapping efficiency, there remains considerable ambiguity with respect to the ideal wettability conditions for capillary trapping (Rabbani et al., 2017). Though a number of experimental and numerical studies argued that brine-wet systems are ideal for CCS (Chalbaud et al., 2009; Iglauer et al., 2011; Chaudhary et al., 2013; Al-Menhali and Krevor, 2016; Herring et al., 2016; Rahman et al., 2016; Al-Khdheeawi et al., 2017; Valle et al., 2018; Rasmusson et al., 2018; Nhunduru et al., 2022; Zhang et al., 2023; Amooie et al., 2024), others have identified that capillary trapping may be significant in intermediate-wet (i.e., neither brine-wet nor CO_2-wet) porous media (Wang and Tokunaga, 2015; Hu et al., 2017; Singh et al., 2017; Purswani et al., 2024). In the overview presented above, experiments performed on core plugs typically exhibit diverse wettability characteristics (Al-Menhali and Krevor, 2016). However, quantifying accurately the in-situ contact angle of core plugs can be a tedious process (Anderson, 1986; Regaieg et al., 2023) and relating the inter/intra pore fluid flow dynamics to the wettability further complicates the entire process. Conversely, numerical studies (example, Nhunduru et al. (2022), Pak et al. (2023) and Purswani et al. (2024)) and microfluidic experiments (example, Hu et al. (2017)) are typically performed under the assumption of homogeneous wettability. This oversimplification related to mono-wet systems within the literature belies the complex spatio-temporal nature of wettability within real reservoir rocks, and in particular, those with a high degree of chemical susceptibility to wettability alteration over geological to production timescales (i.e., mineralogically immature clastics and carbonate reservoir rocks).

Most reservoir rocks targeted for CCS exhibit some degree of wettability heterogeneity (Fig. 1), the origin of which can be attributed to multiple physico-chemical pathways (Blake and De Coninck, 2002; Alhammadi et al., 2017; Regaieg et al., 2023). Buckley et al. (1998) and Okasha et al. (2007) argued that depleted hydrocarbon reservoirs inherit hydrophobicity through oil aging. However, dissolution of CO_2 in brine may reverse the hydrophobicity via the removal of organic residues (Farokhpoor et al., 2013). For brine-CO_2 fluid systems, clean (i.e., phyllosilicate depleted) mineralogically mature sandstones are generally brine-wet (Al-Yaseri et al., 2016). Interactions with dissolved H^+ ions may shift surface chemistry towards mixed-wet behavior, with the presence of clay minerals (i.e., smectite, illite), playing a critical role in wettability alteration due to their high cation exchange capacity and surface charge variability (Chiquet et al., 2007). In similitude, limestones are observed to be generally brine-wet in the context of brine-CO_2 fluid systems. However, acidic brines resulting from CO_2 dissolution can dissolve calcite, exposing fresh mineral surfaces and promoting hydrophobicity through ion bridging (example, Ca^{2+}) potentially causing mixed-wet behavior (Farokhpoor et al., 2013). Shales display perhaps the greatest variance in wettability in the context of brine-CO_2 fluid systems, ranging from water-wet to weakly CO_2-wet due to the presence of organic matter (i.e., kerogen) and clay minerals (Fauziah et al., 2020; Zhou et al., 2022). In addition to mineralogy and lithology, brine geochemistry and the subsurface pressure–temperature ($p-T$) encountered within a CCS site contributes to the development of mixed-wet behavior. For example, high ionic strength and elevated salinity reduces CO_2 solubility, indirectly influencing wetting behavior. Specific ions like Ca^{2+} and SO_4^{2-} may interact with mineral surfaces, stabilizing mixed-wettability states (Arif et al., 2016). Higher p, T increases CO_2 density and surface activity, pushing subsurface systems towards CO_2-wet. The nonpolar CO_2 molecules, particularly in their supercritical state, tend to adsorb onto mineral surfaces, thereby increasing hydrophobicity (Jung and Wan, 2012). It is clear from the above discussion that for numerical investigations looking into the transport dynamics of CO_2 within lithologies targeted for CCS to be of utility, the intrinsic variability in wettability in these rock types should be considered by the modeling workflow. Heterogeneous wettability within geologic pore systems can be classified as either (i). fractional wettability or (ii). mixed wettability.

A fractional-wet porous medium considers two different contact angles θ_1, θ_2 spread across the porous medium in different patterns and may have different percentages of pore occupancy. For brine-scCO_2-sandstone system, Bakhshian and Hosseini (2019) used the lattice Boltzmann (LB) method to study the impact of fractional wettability on the displacement of fluids. The authors found that, dispersed CO_2-wet zones led to more tortuous CO_2 flow paths resulting in increased brine – CO_2 – rock interfacial area that can enhance solubility and mineral trapping. In their study, CO_2 was predominantly trapped in CO_2-wet zones. Using the volume of fluid (VOF) method for air-brine system with different wettability distribution patterns, Jahanbakhsh et al. (2021) observed that fractional wettability produced greater defending phase saturation and distinct displacement behaviors compared to mono-wet systems. Using LB for brine-oil–carbonate rock system, Akai et al. (2019) demonstrated improved agreement with experiments when simulating two-phase flows considering fractional wettability, emphasizing the need to account for heterogeneous wettability. Irannezhad et al. (2023b) further supported this argument through micromodel experiments and pore-scale simulations for similar fluid system. Their study showed oil getting trapped in weakly water-wet zones due to the S-shaped interfacial morphology that develops along the periphery of the zones having different wettability. Extending their findings, Irannezhad et al. (2023a) used dynamic pore network models (PNMs) to reveal that fractional wettability effects are more pronounced at low capillary numbers, influencing both injection pressure and flow structure.

Mixed wettability refers to the porous medium exhibiting a broad distribution of contact angles. Compared to uniform or fractional-wet systems, two-phase flow in mixed-wet porous media remain less explored numerically due to the complexity of representing both pore morphology and wettability heterogeneity (Bakhshian et al., 2020, 2021). Recent studies have begun addressing this gap: Regaieg et al. (2023) and Sedghi et al. (2024) incorporated experimental wettability data from Berea and Bentheimer sandstones into PNMs, showing improved relative permeability predictions over mono-wet models. Using capillary fiber bundles and dynamic PNMs, Fyhn et al. (2021) showed that mixed wettability affects flow rheology in nontrivial ways, challenging assumptions of uniform wetting. In 3D simulations, Guo et al. (2022) compared CO_2-water flow behavior across three mixed-wet regimes. They found that CO_2 trapping decreased as wettability shifted towards intermediate-wet conditions, due to increased access to smaller pores through which CO_2 was able to migrate. While capillary

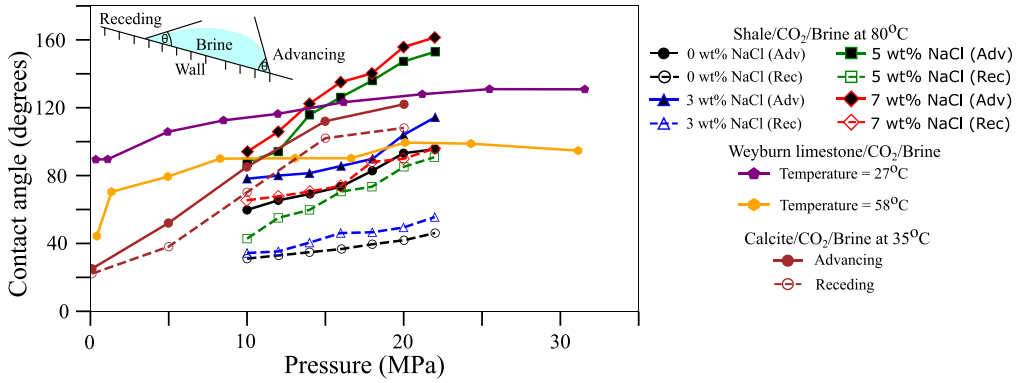

Fig. 1. The diverse range of wettability between CO_2-brine-reservoir rock obtained from laboratory analysis. The wettability data that corresponds to (i). shale/CO_2/brine at temperature $T = 80$ °C for different salinity is from Yekeen et al. (2021), (ii). Weyburn limestone/CO_2/brine at different temperatures is from Yang et al. (2008) and, (iii). calcite/CO_2/brine at $T = 35$ °C is from Arif et al. (2017a).

pressure showed minimal variation, CO_2–water relative permeability was significantly influenced by the wettability distribution.

In this study, to investigate the impact of mixed wettability on immiscible flow dynamics in geological porous media subject to CO_2-brine flooding, we use direct numerical simulations (DNS) on pore systems with randomly distributed wettability characteristics, whereby contact angle ranges from (i). $\Delta\theta = 60(60° \leq \theta \leq 120°)$, (ii). $\Delta\theta = 120(30° \leq \theta \leq 150°)$, (iii). $\Delta\theta = 180(0° \leq \theta \leq 180°)$. This ensures a combination of pore spaces that are wetting $\theta < 90°$, neutral-wet $\theta \approx 90°$ and non-wet $\theta > 90°$ within each studied system. To aid interpretability and promote computational efficiency, we analyze the nature of multiphase flows in two-dimensional porous media. Therein, flows are considered to be viscous dominated, with flow analysis conducted on a complete injection cycle, commencing with injection of a lower viscosity fluid followed by the injection of higher viscosity fluid. The sample-scale fluid displacement morphologies attained for different wetting scenarios are linked to their underlying pore-scale flow mechanisms. Though there exist prior studies related to fluids displacement in mixed-wet systems as mentioned above, our work specifically provides a systematic investigation related to the impact of wettability range on fluid displacement dynamics, ensuring that the mean wettability is consistent across the different systems. This approach allows us to specifically isolate the effect of wettability dispersion on the dynamic nature of fluids displacement, providing insights into how the considered wettability heterogeneity affects phenomena such as viscous fingering and capillary trapping in a controlled and comparable manner.

2. Numerical modeling and simulation setup

2.1. Mathematical model

The incompressible fluid flow dynamics in an isothermal system are governed by the Navier–Stokes equations (NSE) (Versteeg and Malalasekera, 2007). In a multiphase system, instead of solving NSE for each phase independently and coupling the solutions at the interface through boundary conditions, Hirt and Nichols (1981) proposed the volume of fluid (VOF) method in which both the fluids are considered as a single mixture. VOF uses a color function α that indicates the saturation of a specific fluid in a discretized cell. NSE comprises of the mass balance

$$\nabla \cdot \mathbf{U} = 0, \tag{1}$$

and the momentum balance

$$\frac{\partial(\rho\mathbf{U})}{\partial t} + \nabla \cdot (\rho\mathbf{U}\mathbf{U}) = -\nabla p + \nabla \cdot \mu\left(\nabla\mathbf{U} + \nabla\mathbf{U}^T\right) + \mathbf{F}_b + \mathbf{F}_c \tag{2}$$

where $\mathbf{U}$ is the fluid velocity, t is time, p is pressure, $\mathbf{F}_b$ and $\mathbf{F}_c$ are the external body (example, gravity) and capillary forces, respectively. Superscript T denotes a transpose. The fluid density ρ and viscosity μ are computed as $\Psi = \Psi_i\alpha + \Psi_d(1-\alpha)$ where Ψ represents density/ viscosity and the subscripts i, d refer to the invading and defending phases respectively. $\mathbf{F}_c$ at the interfaces are approximated by the continuum surface force (CSF) formulation proposed by Brackbill et al. (1992)

$$\mathbf{F}_c = \sigma\kappa\nabla\alpha \tag{3}$$

where σ is the surface tension between fluids, $\kappa = -\nabla \cdot \frac{\nabla\alpha}{|\nabla\alpha|}$ is the interfacial curvature. Finally, the color function is advected

$$\frac{\partial\alpha}{\partial t} + \nabla \cdot (\mathbf{U}\alpha) = 0. \tag{4}$$

A well known issue using VOF-CSF are the random occurrences of non-physical velocities near the interfaces, referred to as the parasitic currents (PC) (Harvie et al., 2006). Though there exist several methods to alleviate PC for static test cases (Raeini et al., 2012; Albadawi et al., 2013; Shams et al., 2018), there is no conclusive evidence that the proposed methods work for dynamic test cases. In anticipation to eliminate PC, there can arise scenarios where real fluxes can be filtered out (Pavuluri et al., 2018, 2019). Therefore, we use the conventional VOF-CSF method but consider the following remedies to alleviate PC, (i). add an interface compression term $\alpha(1-\alpha)\mathbf{U}_r$ to Eq. (4), (ii). restrict time step size Δt based on the Brackbill number (Brackbill et al., 1992) that has a temporal resolution to capture complex interfacial dynamics such as capillary waves. In the interface compression term mentioned above, $\mathbf{U}_r$ is the compression velocity that acts only at the interfaces and is defined as $\mathbf{U}_r = \min[c_\alpha\mathbf{U}_{cv}, \max(\mathbf{U}_d)]$ where c_α is a compression coefficient, $\mathbf{U}_{cv}$ and $\mathbf{U}_d$ refer to the fluid velocities in the control volume and entire domain respectively (Rusche, 2002). Based on the studies by Deshpande et al. (2012), Hoang et al. (2013), Ferrari and Lunati (2013) we set $c_\alpha = 1$. The interface compression term assists in alleviating numerical diffusion that arises while solving Eq. (4) thereby, reducing the number of cells around an interface effected by PC. Refer to Section 2.3 regarding the Brackbill time step used for the simulations.

2.2. Simulation setup

2.2.1. Porous medium

Fig. 2a shows the porous medium used for analysis in this study. The considered porous medium is 40.1 mm wide (horizontal) and 18.2 mm in height. The porosity is $\phi = 57.56\%$. Non-overlapping circular grains having a uniform diameter are randomly placed covering the entire rectangular region except in the buffer zone near the left boundary. The buffer zone is 2.6 mm wide where the circular grains are distributed in a uniform pattern. The buffer zone is considered to alleviate boundary

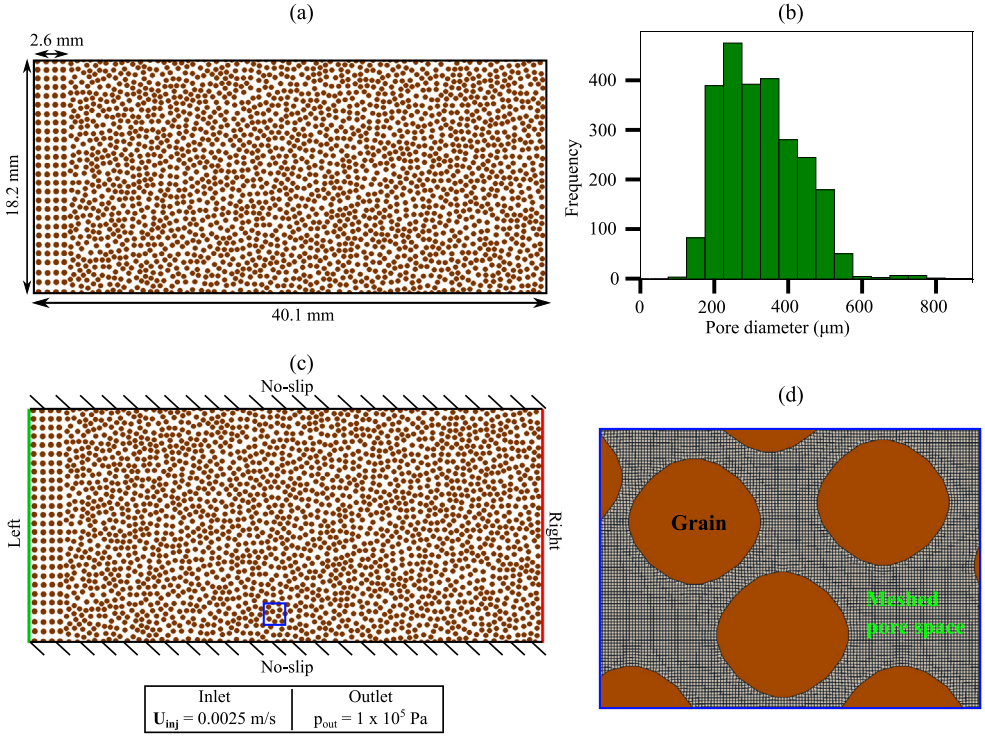

Fig. 2. (a) The porous medium used for investigation in this study. The grains are shown in brown and the pore spaces are represented in white. (b) Pore size distribution of the porous medium shown in (a). (c) The boundary conditions used for the simulations. We investigate two flooding scenarios. For the first injection cycle, left and right boundaries serve as inlet and outlet respectively. For the second injection cycle, right and left serve as inlet and outlet respectively. The blue square highlighted in (c) is magnified in (d) to reveal the meshed pore space. (For interpretation of the references to colour in this figure legend, the reader is referred to the web version of this article.)

effects, i.e., to avoid direct and forceful injection of fluids into the porous medium comprising of randomly distributed grains. The pore size distribution of the porous medium excluding the buffer zone is shown in Fig. 2b. Most pores have diameter in the range 200–400 μm. The pore sizes are calculated using distance transform watershed algorithm followed by fitting the segmented pore spaces by the maximum circle that can be inscribed within. Fiji's MorpholibJ library (Legland et al., 2016) is used to calculate the pore sizes. In the manuscript, we do not exclusively distinguish between pore bodies and pore throats and in general refer to them as pores. Refer to Section 1 of the supporting information (SI) that showcases the segmented pore spaces and the circles inscribed within them.

The highlighted blue square in Fig. 2c is magnified and shown in Fig. 2d to reveal the meshed pore spaces. The entire rectangular domain 40.1 mm × 18.2 mm, Fig. 2(a) is initially discretized by Cartesian cells having dimension $\Delta x = \Delta y = 10$ μm. On these Cartesian cells, OpenFOAM's snappyHexMesh library is used to remove the grains and mesh only the pore space. The final mesh comprises of Cartesian cells far away from the grain boundaries, and, snapped cells near the grain boundaries which capture the pore morphology. A total of 4.2 millions cells are used to capture the entire pore space. The mesh resolution used in this study $\Delta x = 10$ μm was chosen based on the geometric resolution required to capture the pore morphological features and considering the computational capabilities. While a resolution of $\Delta x = 12.5$ μm with 2.5 millions cells was unable to resolve several narrow pore throats between closely packed grains, these pore morphological intricacies were captured at a resolution $\Delta x = 10$ μm in which majority of the narrow pore throats were discretized by at least three cells and a few very narrow throats were discretized by two cells. At a refinement of $\Delta x = 8$ μm with 7 million cells, there still exist relatively fewer narrowest pore throats discretized by 2 cells. Considering the significant increase in the computational costs trying to resolve these geometric intricacies and acknowledging the inherent relation that finer meshes result in smaller time step sizes (refer to Section 2.3), we adopted $\Delta x = 10$ μm as the optimal balance between geometric fidelity and computational feasibility.

2.2.2. Fluid properties and flooding procedure

We distinguish the two fluids in the porous medium based on their viscosity as low viscous fluid (LV) and high viscous fluid (HV). LV has a viscosity of $\mu_{LV} = 1 \times 10^{-4}$ $\frac{\text{kg}}{\text{ms}}$ and HV has a viscosity of $\mu_{HV} = 1 \times 10^{-1}$ $\frac{\text{kg}}{\text{ms}}$. The interfacial tension between LV and HV is $\sigma = 0.07$ $\frac{\text{kg}}{\text{s}^2}$. The density of both fluids are $\rho = 1000$ $\frac{\text{kg}}{\text{m}^3}$. As there is no density difference, gravity is ignored in this study.

We initially saturate the porous medium with LV, approximately by 5% - from the left boundary shown in Fig. 2c up to 1.3 mm in the buffer zone. The top and bottom boundaries of the rectangular domain along with the surface of the soil grains are assigned a no-slip boundary condition, i.e., $\mathbf{U} = 0$ $\frac{\text{m}}{\text{s}}$. We perform two injection cycles resembling the experimental works of Pentland et al. (2011) and El-Maghraby and Blunt (2013). In the first injection cycle, LV is flooded from left to right (see Fig. 2c) until breakthrough. The fluid invasion morphology at breakthrough is preserved and the second injection cycle commences where HV is injected into the porous medium from right to left. HV flooding is performed until steady-state conditions are reached, i.e., until no further changes in the fluid configurations are noticed. Therefore, both the left and right boundaries in Fig. 2c serve as inlet and outlet, depending on the injection cycle. Irrespective of the injection cycle, the inlet boundary is subjected to a continuous injection of the invading phase at a fixed velocity, $\mathbf{U}_{\text{inj}} = 0.0025$ $\frac{\text{m}}{\text{s}}$. The corresponding outlet boundary is subjected to a fixed pressure, $p_{\text{out}} = 1 \times 10^5$ Pa.

The dimensionless capillary number Ca, defined as the ratio between viscous forces to capillary forces is $Ca = \frac{U_i \mu_{max}}{\sigma} = 3.57 \times 10^{-3}$ indicating that the flows being investigated in this study are viscous dominated. Viscosity ratio M is another dimensionless number that defines the ratio between viscosity of invading to defending phases,

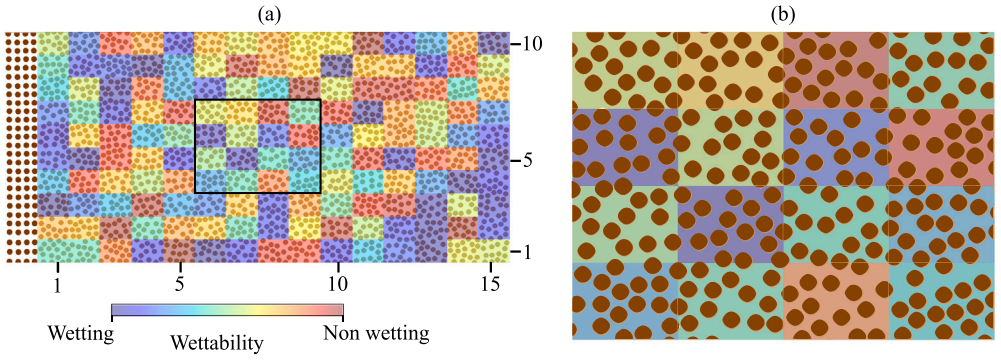

Fig. 3. (a) An illustration of the porous medium (shown in Fig. 2a) overlaid by the wettability distribution. A set of 150 different contact angles are randomly assigned to the pore spaces. The pore spaces underlying blue regions indicate imbibition zones i.e., $\theta < 90°$. The pore spaces underlying red regions indicate drainage zones i.e., $\theta > 90°$. The highlighted rectangular region in the center of the porous medium is magnified and shown in (b). The contact angle in the buffer zone (2.6 mm from the left boundary) is always fixed at $\theta = 90°$. (For interpretation of the references to colour in this figure legend, the reader is referred to the web version of this article.)

$M = \frac{\mu_i}{\mu_d}$. During LV flooding, $M = 0.001$ and during HV flooding, $M = 1000$.

2.2.3. Wettability distribution

We assign mixed-wet conditions for the porous medium described in Section 2.2.1. Fig. 3a illustrates the wettability distribution of the porous medium. The porous medium excluding the buffer zone is segregated into 150 cells: 15 columns and 10 rows. Contact angles for the 150 cells are randomly assigned keeping a constraint that the average of the 150 values is $\theta_a = 90°$. We consider three mix-wet cases having different standard deviations in the wettability. Cases mentioned in the ascending order of standard deviation are (i). $\Delta\theta = 60$ with the contact angles in the range $60° \leq \theta \leq 120°$, (ii). $\Delta\theta = 120(30° \leq \theta \leq 150°)$, and, (iii). $\Delta\theta = 180(0° \leq \theta \leq 180°)$. The choice of the mentioned wettability ranges helps us to investigate the sensitivity of multiphase flows (related to the trapping efficiency, flow morphology and ganglia dynamics) with respect to the chosen wettability contrasts. Though $\Delta\theta = 180$ might seem extreme, corresponding wettability ranges (0°–165° for brine-CO_2-Bentheimer sandstone) were identified in the experimental study of Herring et al. (2021) across different drainage-imbibition cycles. $\Delta\theta = 120$ illustrates the in-situ contact angle (θ in range 40°–145° for brine-CO_2-sandstone) measured using micro X-ray CT in the work of Tudek et al. (2017). Finally, $\Delta\theta = 60$ narrows the wettability heterogeneity that typically occurs in reservoirs having low organic content (Arif et al., 2017b). To ensure reproducibility of the wettability distribution in the porous medium, we employed a fixed random seed number to assign 150 contact angle values having a mean of 90°. The same seed was used across all three mixed-wet cases to ensure that the spatial pattern of wettability heterogeneity remains consistent across cases — i.e., a given region that is non-wet in one scenario will remain non-wet in the others. However, the specific contact angle value in each region will vary according to the selected wettability range $\Delta\theta$. This method allows us to isolate the effect of varying wettability range while maintaining a consistent underlying spatial structure, facilitating a clearer interpretation of wettability effects on the flow behavior. All through this study, θ refers to the contact angle made by LV with the solid surfaces in the presence of HV. In Fig. 3, the pore spaces overlaid by blue indicate imbibition zones with $\theta < 90°$ (LV-wet), green represents neutral-wet regions with $\theta \approx 90°$ and red represents drainage zones with $\theta > 90°$ (HV-wet). In Fig. 3a, a rectangular region at the center of the porous medium is highlighted which is magnified and shown in Fig. 3b.

It has been observed through sessile drop and tilted plate experiments that the porous medium turns to strong CO_2-wet as the total organic content in the rocks increase (Iglauer et al., 2015; Arif et al., 2017b; Pan et al., 2018). The presence of organic content in the subsurface at multiple locations eventually elevates the mean wettability towards neutral-wet. Tudek et al. (2017) measured the in-situ contact angle of a brine-CO_2-sandstone system using micro X-ray CT and observed that the mean wettability of the sample was around 90° (measured in-situ range of θ: 40°–145°). Though the authors in Tudek et al. (2017) acknowledged that the reported mean wettability is relatively higher than those reported in literature, the authors aligned their observations with respect to the findings of Iglauer et al. (2015) who argued such neutral-wet conditions can occur in the presence of hydrocarbon impurities. The above studies confirm that real subsurface systems do exhibit neutral-wet conditions ($\theta_a \approx 90°$) and therefore are required to be investigated.

2.3. Numerical model

The cases described above have been modeled in the OpenFOAM® software. The VOF-CSF based multiphase flow solver interFoam is used for running the simulations. OpenFOAM® is built on the finite volume method framework (Jasak, 1996) with the field variables — $p, \mathbf{U}, \alpha$ stored at the cell centers. The pressure implicit with splitting of operators (PISO) algorithm proposed by Issa (1986) is used to solve for $p, \mathbf{U}$ from Eqs. (1), (2). The computed $\mathbf{U}$ is then used in Eq. (4) to advect α and get the updated fluid configurations. A first order Euler time discretisation and second order Gauss linear scheme for the gradient terms in Eq. (2) are used. The advection term in Eq. (2) — second term on the left hand side, is solved using limited linear difference. The vanLeer scheme (Van Leer, 1974) is used to advect α in Eq. (4). The time step size Δt is computed as $\Delta t = \min(\Delta t_{Co}, \Delta t_{Bk})$. The subscript Co refers to the Courant number $Co = \frac{U\Delta t_{Co}}{\Delta x}$ (Courant et al., 1928) set to 0.3 in this study. Δt_{Bk} is the Brackbill time step computed as $\Delta t_{Bk} = \sqrt{\frac{\rho_a(\Delta x)^3}{\pi\sigma}}$ (Brackbill et al., 1992). ρ_a refers to the average fluid density in a control volume. All simulations were run in parallel on 48 Intel Xeon 2.60 GHz processors and it took approximately 4 weeks to model the entire cycle of injections (i.e., both LV and HV flooding) for a single $\Delta\theta$.

3. Results and discussion

3.1. First half of the injection cycle: Flooding by the less viscous fluid

3.1.1. LV flooding in a uniform-wet porous medium

The considered contact angle for analysis in this section is $\theta = 90°$, similar to the average contact angle θ_a of the mixed-wet cases discussed in the next section. Throughout this study, we refer to this case as $\Delta\theta = 0$ indicating a zero standard deviation of wettability. At a low $M = 0.001$ and relatively high $Ca = 3.57 \times 10^{-3}$, fluid displacement in the porous medium is mainly governed by the viscous forces, promoting invasion in the form of viscous fingering (Lenormand et al., 1988). The invasion profile of LV in the porous medium is shown in Fig. 4a.

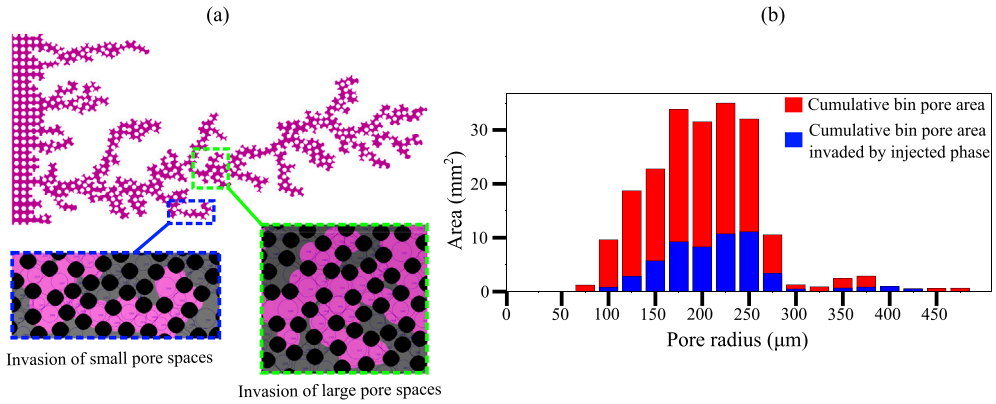

Fig. 4. LV flooding for $\Delta\theta = 0$. (a) shows the invasion morphology of LV in pink. White corresponds to the combination of grains and pore spaces occupied by HV. The highlighted blue and green boxes show invasion of LV through relatively small and large pore spaces respectively. (b) The total pore area in red and the LV invaded pore area in blue are shown as a function of pore size. (For interpretation of the references to colour in this figure legend, the reader is referred to the web version of this article.)

Indeed, we observe that LV propagates through the porous medium in the form of elongated and tortuous finger like protrusions. The invasion morphology is composed of several fingers of varying lengths and widths. Whilst some of the independent fingers form, grow and arrest, there exists one specific finger through which LV preferentially flows, acting as a conduit across the porous domain connecting the inlet to the outlet. Along the length of this terminal finger, many secondary fingers are seen to branch out. Ferrari et al. (2015) compared numerical simulations (DNS-VOF) with micromodel experiments for air–water-cylindrical obstacles system considering uniform wettability $\theta = 30°$ at $Ca = 8 \times 10^{-5}$. Their study reported approximately 80% similarity in the viscous fingering morphology comparing the 2D simulation with experiment. The remaining discrepancy was attributed to differences in initial conditions, uncertainties in pore-scale geometry, and limitations in capturing certain 3D flow features in a 2D framework — despite the inclusion of an additional term in the NSE to mimic viscous dissipation across the micromodels width. Qualitatively, we identify similarities between our results and Ferrari et al. (2015) with respect to the displacement patterns involving branching of secondary fingers from the terminal finger. A signature of the viscous fingering flow regime is the invasion of pore bodies of different size by the invading fluid (Pavuluri et al., 2023) as shown in Fig. 4a. The same observation is quantified in terms of the LV invasion area against pore size in Fig. 4b at the time of breakthrough, within which a combination of small and large pores are seen to be invaded by LV. To obtain the bin pore area and the bin pore area invaded by LV shown in Fig. 4b, initially the pores obtained through fitting maximum circles in segmented pore spaces through distance transform watershed method are classified into respective bins based on their radius. For each pore, their respective area is approximated as πr_p^2 where r_p is the radius of the maximum inscribed circle in the segmented pore space. To determine the cumulative bin pore area, we sum all the pore areas that belong to a specific bin. To determine the bin pore area invaded by LV, we select all pores that are at least 50% invaded by LV, calculate those respective pores area as πr_p^2 and sum only these pore areas invaded by LV for each bin. Refer to Section 2a of the SI for further details related to the LV invasion area calculation for $\Delta\theta = 0$.

3.1.2. LV flooding in a mixed-wet porous medium

The invasion profiles of LV at the time of breakthrough during LV flooding for different mixed-wet cases, (i). $\Delta\theta = 60$, (ii). $\Delta\theta = 120$ and (iii). $\Delta\theta = 180$ are summarized in Fig. 5. The flow morphology for the mixed-wet cases is compared against the reference case $\Delta\theta = 0$ to visually distinguish between the flow patterns. From Fig. 5a, b, c it can be observed that irrespective of the wettability regime, viscous fingering always occurs. However, it can be observed that fingering patterns vary among the studied wettability distributions, a qualitatively similar finding from the study by Trojer et al. (2015) where the authors identified different viscous fingering patterns by tuning the wettability of the micromodels (multiple experiments with different mono-wet conditions were performed) at similar Ca. For the mixed-wet cases investigated in this study, though the invasion profiles close to the inlet boundary match with the invasion profile seen for $\Delta\theta = 0$, the flow heterogeneity is visible as the flow develops. Section 3 of the SI quantifies the percentage of overlay of LV flow morphology between the mixed-wet cases and $\Delta\theta = 0$ along the entire flow length. As $\Delta\theta$ increases, we notice that the branches from the terminal finger (i.e., the finger connecting the inlet and outlet) form cluster like patterns, especially for $\Delta\theta = 180$. The zones favored for LV invasion are quantified in Fig. 5d, e, f for different mixed-wet cases. In Fig. 5d, e, f the available pore area and the LV invaded pore area are shown as a function of the wettability. The entire range of wettability for the mixed-wet cases are split into 6 bins having equal interval sizes i.e., for $\Delta\theta = 60$ — the bin interval is 10, for $\Delta\theta = 120$ — the bin interval is 20 and for $\Delta\theta = 180$ — the bin interval is 30. For each of the mixed-wet cases, moving from bin 1 to bin 3 signifies a relative decrease in the LV wettability, whereas, moving from bin 4 to bin 6 signifies an increase in the HV wettability (or increase in the LV non-wetting states). To calculate the bin pore area and bin pore area invaded by LV shown in Fig. 5d, e, f, we initially split the porous medium having mixed wettability into 150 cells and label them by their row and column ID as shown in Fig. 3a. A Fiji macro is created that loops over all the 150 cells to output the pore area of each cell. As the wettability of each cell is apriori know, we classify the cells into respective bins according to their contact angle. Then, we sum the pore area of each cell in a bin to get the bin specific pore area. The same procedure however, using the LV invasion profile is used to get the bin specific pore area invaded by LV. For this, the invaded area by LV for each of the 150 cells is calculated using a Fiji macro. Corresponding cells that belong to a specific bin (based on the contact angle) are collected, and the LV invaded pore areas are summed up. Refer to Section 2b of the SI for a detailed explanation of the same. In general, we can observe that LV prefers to invade the wetting (imbibition, $\theta < 90°$) zones compared to the non-wetting (drainage, $\theta > 90°$) regions. This behavior becomes more pronounced as $\Delta\theta$ increases. In the imbibition zones, comparing the pore area invaded by LV for different $\Delta\theta$, we notice a trend where, $\Delta\theta = 180 > \Delta\theta = 120 > \Delta\theta = 60$. The trend reverses in the drainage zone where the pore area invaded by LV is relatively more for $\Delta\theta = 60$ followed by $\Delta\theta = 120$ and $\Delta\theta = 180$ respectively. Refer to Section 4 of the SI to see the bin specific saturation of LV calculated as $S_{LV} = \frac{\text{pore area invaded by LV of a bin}}{\text{pore area of a bin}}$ for all $\Delta\theta$. In Section 4 of the SI we overlay the LV invasion profiles shown in Fig. 5a, b, c with the imbibition and drainage zones of the porous medium to highlight the

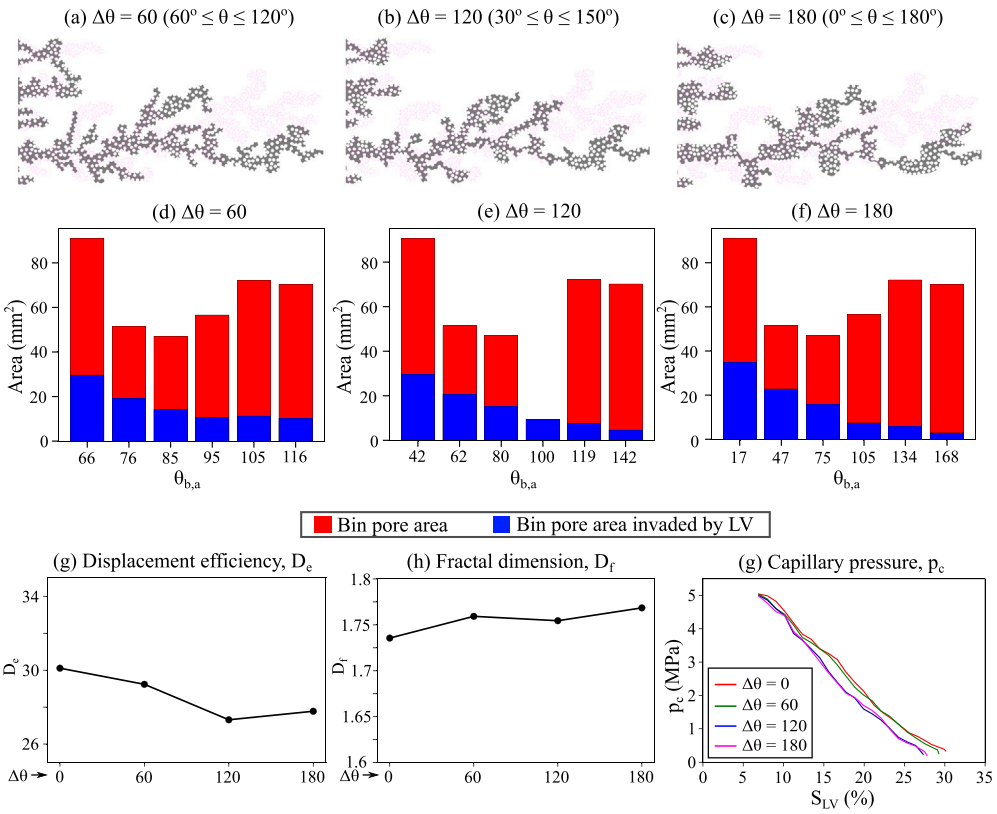

Fig. 5. LV flooding in mixed-wet porous medium. The LV invasion morphology for (a) $\Delta\theta = 60$, (b) $\Delta\theta = 120$ and (c) $\Delta\theta = 180$ is show in black. The pink outline in (a), (b), (c) corresponds to the LV invasion for $\Delta\theta = 0$ shown for visual comparison of the invasion patterns. Fig. 5(d), (e) and (f) show the bin specific pore area in red and the LV invaded pore area in blue as a function of wettability for $\Delta\theta = 60, 120, 180$ respectively. For each specific $\Delta\theta$, the range of θ is split into 6 bins having equal interval sizes and the average of the bin specific contact angle is referred by $\theta_{b,a}$. The LV invasion morphology is quantified by the displacement efficiency D_e in (g), the fractal dimension D_f in (h) and the capillary pressure p_c against LV saturation S_{LV} in (g). The p_c in (g) is measured at an interval of 0.1s. As we consider an initial LV saturation of 5% in the porous medium, p_c is computed from $S_{LV} \approx 5\%$. (For interpretation of the references to colour in this figure legend, the reader is referred to the web version of this article.)

pore spaces invaded by LV. While LV preferentially invades through the imbibition zones, we observe that LV invasion through the drainage zones are of two types: (i). LV enters the drainage zone as fingers and perturbs further invasion, and (ii). LV enters the drainage zones as a thin finger that conducts the invading phase to neighboring imbibition zones or to a relatively less strong non-wetting drainage zones.

The flow morphology attained during LV flooding for all $\Delta\theta$ is quantified by the displacement efficiency D_e shown in Fig. 5g and by the fractal dimension D_f shown in Fig. 5h. D_e indicates the saturation of LV (S_{LV}) at the time of breakthrough calculated as

$$S_{LV} = \frac{A_{LV}}{A_p} \tag{5}$$

where A_{LV} is the total pore area invaded by LV and A_p is the available pore area in the porous medium. Fiji is used to calculate both A_{LV}, A_p. D_f indicates the geometrical characteristics of the invasion front and is calculated using the box counting method proposed by Feder (1988),

$$D_f = -\frac{d(\log N(r))}{d(\log(r))} \tag{6}$$

where r refers to the box size and $N(r)$ refers to the number of boxes. D_f was approximated by performing linear regression on the log–log plot of r versus $N(r)$. $D_f = 1$ indicates a highly non-uniform invasion fronts, whereas, $D_f = 2$ indicates a uniform and smoother invasion fronts. A general trend that we observe as $\Delta\theta$ increases is that, the D_e marginally drops and D_f marginally increases. The numerical and experimental study by Ferrari et al. (2015) reported $D_f \approx 1.7$ for viscous fingering in a mono-wet heterogeneous porous medium drawing close comparison with the D_f reported in our study $D_f \approx 1.75$. It is interesting that, even though the invasions patterns vary among the investigated $\Delta\theta$, the impact of the flow morphology on D_e and D_f are not significant. The breakthrough times for the investigated cases in this study range from $t_b \approx 2.1$ s–2.4 s with the lower ranges of t_b mentioned are for mixed-wet cases having larger wettability contrast i.e., $\Delta\theta = 120, 180$. The higher ranges of t_b correspond to cases with lower wettability contrasts $\Delta\theta = 0, 60$. As the porous medium and the injection rates used for all investigated cases are similar, the differences in t_b reflect on the tortuous flow paths taken by the invading fluid i.e., longer t_b corresponds to relatively more tortuous path taken by the invading fluid compared to cases with lower t_b. Additionally, t_b also impacts D_e ($t_b \propto D_e$). Fig. 5h shows the evolution of capillary pressure p_c as a function of S_{LV}. p_c is computed as

$$p_c = p_i - p_d \tag{7}$$

where p_i and p_d are the invading and defending phase pressures respectively computed as volumetric averages. For example, p_i is calculated as

$$p_i = \frac{\sum p_i V_i}{\sum V_i} \tag{8}$$

where V_i refers to the volume of the cell occupied by the invading fluid. As a less viscous fluid is continuously invading the porous medium and displacing out the resident viscous fluid, the p_c continuously reduces as S_{LV} increases. We notice that the drop in p_c is relatively more pronounced for the larger wettability contrast cases ($\Delta\theta = 120, 180$) compared to the cases with lower wettability contrasts. This observation reflects the enhanced capillary heterogeneity for the larger wettability contrast cases that resulted in relatively less tortuous preferential flow paths and relatively faster fluid-fluid interfacial reconfigurations that keep continuously occurring at the pore-scale. In the next section, we attempt to link the sample-scale flow observations presented above with the pore-scale flow physics.

3.1.3. Pore-scale flow phenomena during LV flooding

The sample-scale LV invasion morphology discussed in Sections 3.1.1 and 3.1.2 are a consequence of fluid displacement occurring at the pore-scale. In this regard, we investigate the manner in which LV invades through a finite number of pore spaces for different $\Delta\theta$. For analysis, we consider a specific region in the investigated porous medium that is invaded by LV in all of the investigated $\Delta\theta$ cases. The region of interest as shown in Fig. 6 comprises of four different wettability distributions. In the region of interest, one quarter of the pore spaces are neutral-wet (bottom left), another quarter of the pore spaces are intermediate non-wet (top left), and remaining half region is strongly wetting to LV (right side). Fig. 6 shows snapshots of LV invasion for different $\Delta\theta$. Starting with $\Delta\theta = 0$, we see that the invading fluid penetrates through the porous medium in the form of unstable bursts. As a consequence, pores of different sizes are invaded by LV. However, the narrowest of the pore spaces are typically bypassed during the invasion process for $\Delta\theta = 0$. This is because the narrowest pore spaces correspond to regions having the greatest viscous dissipation and hence, the fluids prefer to flow through pore spaces that offer relatively lower viscous resistance. In the region of interest, for all the mixed-wet cases, i.e., $\Delta\theta > 0$, we notice that the LV invasion commences through the non-wetting zone (top left). For all of the mixed-wet cases, LV is never seen to invade through the neutral-wet zone (bottom left). For $\Delta\theta = 60$, as LV invades through the non-wet pore spaces in the form of bursts, the formation of a finger that protrudes horizontally can be observed. As LV enters the wetting (imbibition) region, LV commences to progressively spread over the grain surface and is subjected to cooperative pore filling. During cooperative pore filling, multiple menisci merge together to form a single meniscus (Zacharoudiou et al., 2017). At times, even a stagnant meniscus can merge with a neighboring meniscus in motion to form a new meniscus promoting continued imbibition through the porous medium. As $\Delta\theta$ increases to $\Delta\theta = 120$ and 180, the relative strengths of drainage and imbibition in the non-wetting and wetting zones increase respectively. This observation has a direct impact on (i). the length of finger development, and (ii). the quantities of LV imbibed in the wetting zones as a consequence of cooperative pore filling. In general, as $\Delta\theta$ increases, the length of finger developed in the non-wetting zone reduces and a greater portion of the wetting zones are invaded by LV. Interestingly, for $\Delta\theta = 180$, we notice that the finger initially developed in the non-wetting zone retracts completely and migrates into the surrounding imbibition zones, indicating that finger retraction assists in cooperative pore filling. Similar sort of flow dynamics were observed in the study by Aziz et al. (2019) while investigating oil recovery from pore spaces during low salinity water flooding in a heterogeneous porous medium. In Aziz et al. (2019), the wettability in the porous medium was varied as a function of salts concentration: $\theta = 140°$ for high-saline water and $\theta = 30°, 60°$ for low-saline water. It was observed in their pore-scale simulations that the high-saline water (corresponds to large θ) pulls (retracts) back filling surrounding pores occupied by low-saline water consequently pushing out the oil in the neighboring pore spaces. The flow mechanisms observed in Fig. 6 as a consequence of differences in the relative strengths of drainage and imbibition at the pore-scale, reflect the flow patterns seen at the sample-scale (Fig. 5d, e, f) in which we notice differential wetting zones being invaded by LV.

3.2. Second half of the injection cycle: Flooding by the viscous fluid

3.2.1. Capillary trapping in a mixed-wet porous medium

For all $\Delta\theta$, the LV breakthrough configurations attained during LV flooding (see Sections 3.1.1, 3.1.2) were used as initial conditions while commencing the HV flooding. Therefore, HV flooding is done in the porous medium co-occupied by both LV and HV. For $M = 1000$ and $Ca = 3.57 \times 10^{-3}$, we expect a compact displacement of HV through the porous medium (Lenormand et al., 1988). During compact displacement, the invading fluid forms a stable front while displacing the defending phase. As a consequence, D_e is usually much larger compared to D_e during viscous fingering (Pavuluri et al., 2023). During this displacement process, the defending LV phase gets trapped in the pore spaces due to capillary effects. When the pressure of the invading fluid cannot overcome the capillary entry pressure of a pore space, the defending fluid in that specific porous region is bound to remain trapped. It is intriguing to identify the locations in the mixed-wet porous medium where LV gets immobilized and further quantify the saturation behavior of the porous medium which depend on the sizes of the trapped ganglia. Simulations were run until steady-state conditions were achieved, i.e., no further migration of the existing ganglia and no changes in the saturation were observed. Steady-state during HV flooding typically occurs after breakthrough, as ganglia dynamics can continue post breakthrough.

The trapped LV at steady-state for different $\Delta\theta$ is shown in Fig. 7a, b, c. It is clear from Fig. 7a, b, c that the sizes of the trapped LV ganglia vary as a function of $\Delta\theta$, varying from isolated ganglia within narrow pore spaces to large clusters across protracted porous zones. The trapped defending phase is quantified in Fig. 7d, e, f which show the distribution of pore area containing trapped LV for different $\Delta\theta$. The same procedure explained in Section 3.1.2 is used here to determine the bin specific pore area trapped with LV. The corresponding bin specific pore areas are similar to those shown in Fig. 5d, e, f for different $\Delta\theta$. The bin specific saturation of trapped LV for different $\Delta\theta$ can be seen in Section 5.1 of the SI. Results suggest, as $\Delta\theta$ increases, the quantity of LV trapped in the LV wetting zones increases commensurately. On the other hand, the quantity of LV trapped in the LV non-wet zones are minimal and of similar quantities for all $\Delta\theta > 0$. Refer to Section 5.2 of the SI to see the entrapped LV ganglia overlaid on the drainage and imbibition zones. Similar to the observations presented above where substantial quantities of LV get trapped in the LV-wet zones, Bakhshian and Hosseini (2019) who numerically investigated CO_2 trapping in a fractional-wet porous medium also noticed greater entrapment of CO_2 in CO_2-wet zones. The experimental studies by Herring et al. (2021) on Bentheimer sandstone supplement the arguments put forth by the numerical models. In Herring et al. (2021), the authors performed several cycles of CO_2-brine injections and noticed a change in the wetting state towards mixed-wet and identified that the trapping efficiency of CO_2 has increased as the porous medium turns into a patchy mixed-wet state rendering the CO_2 trapped in the CO_2-wet zones as relatively more stable.

Whilst some ganglia in Fig. 7 are formed during HV flooding, other ganglia form over protracted periods of time, subject to ganglia dynamics. These ganglia dynamics include the breaking up of a large ganglia, or the migration of a ganglia followed by coalescence with a stranded ganglia causing interfacial reconfigurations followed by further displacements (Rücker et al., 2015). Fig. 8 shows how the ganglia dynamics evolve over time during HV flooding, with ganglia count and sizes quantified. The simulation outputs related to the flow morphology at different time intervals are analyzed in Fiji to obtain the results presented in Fig. 8. The flow profiles at different times are initially binarized such that the LV phase is represented in white and black represents the combination of grains and the HV phase. We use Fiji's analyze toolkit to obtain essential information related to the ganglia count presented in Fig. 8a, area of each ganglia which we sum and divide by the ganglia count to obtain the average ganglia size with respect to time presented in Fig. 8b, c. The same toolkit is used on the output of the last time step i.e., at steady-state, to extract data related to the steady-state ganglia size distribution presented in Fig. 8d–g. Refer to Sections 5.3, 5.4 of the SI for a detailed overview on the procedure followed to extract the metrics presented in Fig. 8. Among the investigated cases, $\Delta\theta = 0$ shows a delayed breakthrough but reached steady-state almost instantaneously after breakthrough (see Fig. 8a). However, for the mixed-wet cases, we see an early breakthrough whereby there exists a lag for the flow dynamics to reach steady-state. At steady-state, $\Delta\theta = 0$

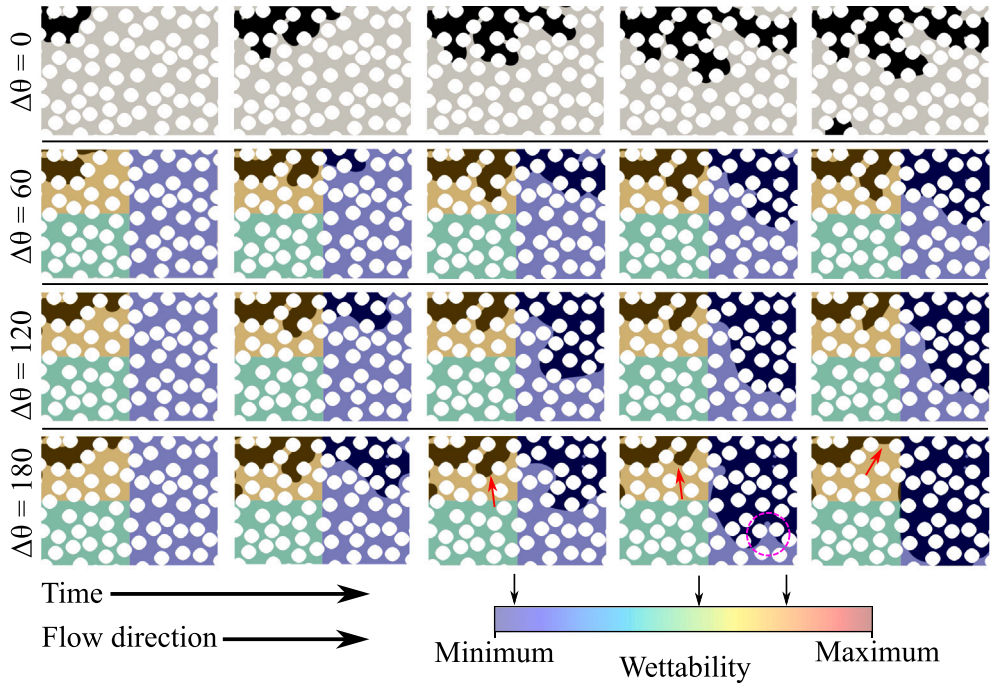

Fig. 6. A pore-scale perspective of LV invasion through a porous region having mixed-wettability for different cases of $\Delta\theta$. The region of interest in this figure corresponds to the cells $7\times2, 7\times3, 8\times2, 8\times3$ for reference (see Fig. 3a, Section 4.3 of the SI). The invasion profile of LV is shown in black as snapshots. The porous medium comprises of a non-wet region (region highlighted in brown, top left), 2 wetting regions (region highlighted in blue, right side) and a neutral-wet region (region highlighted in green, bottom left). The arrows on the generalized wettability scale indicates the wettability for specific $\Delta\theta$ cases. The impact of increasing $\Delta\theta$ on, (i). the finger length in the non-wet zone, (ii). increased imbibition in the wetting zones due to cooperative pore filling can be observed. For $\Delta\theta = 180$, the highlighted red arrows show finger retraction and the pink circle shows 3 different menisci which eventually merge to form a single meniscus and cooperatively fill the pore spaces. (For interpretation of the references to colour in this figure legend, the reader is referred to the web version of this article.)

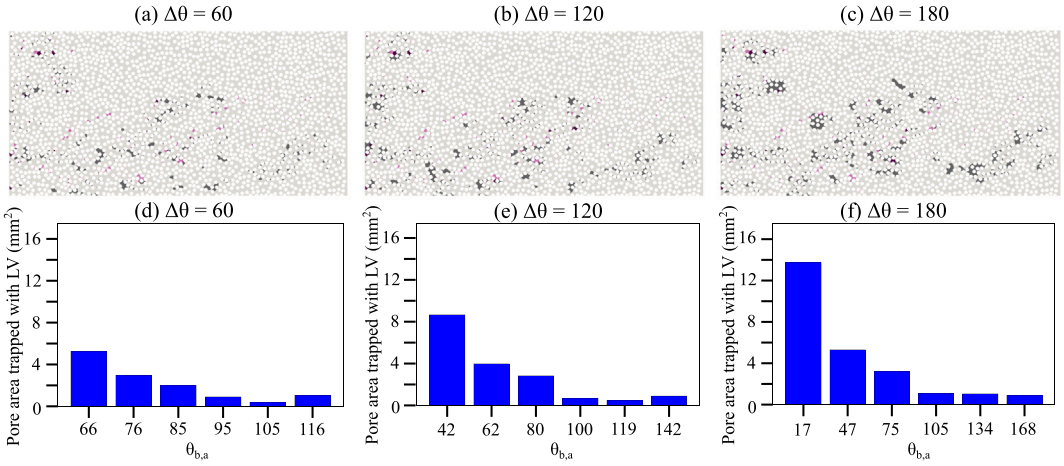

Fig. 7. Trapped defending LV phase at steady-state shown in black for (a) $\Delta\theta = 60$, (b) $\Delta\theta = 120$, (c) $\Delta\theta = 180$. For (a), (b), (c) we overlay the trapped LV phase seen for $\Delta\theta = 0$ which is shown in pink for comparison. The pore area trapped with LV for (d) $\Delta\theta = 60$, (e) $\Delta\theta = 120$, (f) $\Delta\theta = 180$ are shown. The bin specific available pore area can be seen in Fig. 5d, e, f. (For interpretation of the references to colour in this figure legend, the reader is referred to the web version of this article.)

exhibited the lowest number of ganglia (see Fig. 8a) and also had the smallest average ganglia size (see Fig. 8b, c). Conversely, for all the mixed-wet cases, there were approximately an equal number of ganglia formed (Fig. 8a), though the average ganglia size (at steady-state) increased commensurately with $\Delta\theta$ (see Fig. 8b,c). This observation can be explained by looking at the evolution of the cumulative distribution function (CDF) with respect to the ganglia size shown in Fig. 8d–g. The CDF of $\Delta\theta = 180$ shows evidence of divergence as $\Delta\theta$ reduces. This behavior indicates, compared to $\Delta\theta = 180$, there are a greater number of smaller sized ganglia and lower number of large sized ganglia as $\Delta\theta$ reduces.

Metrics related to the capillary trapping of LV at the sample-scale for different $\Delta\theta$ are presented in Fig. 9. Fig. 9a compares the initial LV saturation $S_{LV,i}$ present at the start of HV flooding against the final/ trapped LV saturation $S_{LV,r}$ present at the end of HV flooding. In general, as $\Delta\theta$ increases, HV flooding commences with a lower $S_{LV,i}$. Though larger $\Delta\theta$ is associated with lower $S_{LV,i}$, after HV flooding, the quantities of $S_{LV,r}$ are relatively larger compared to cases with low $\Delta\theta$. This sample-scale observation can be linked to the ganglia size distribution shown in Fig. 8d–g where larger ganglia are trapped as $\Delta\theta$ increases. The trapping efficiency η is a parameter that links $S_{LV,i}$ and $S_{LV,r}$ as

$$\eta = \frac{S_{LV,r}}{S_{LV,i}}. \tag{9}$$

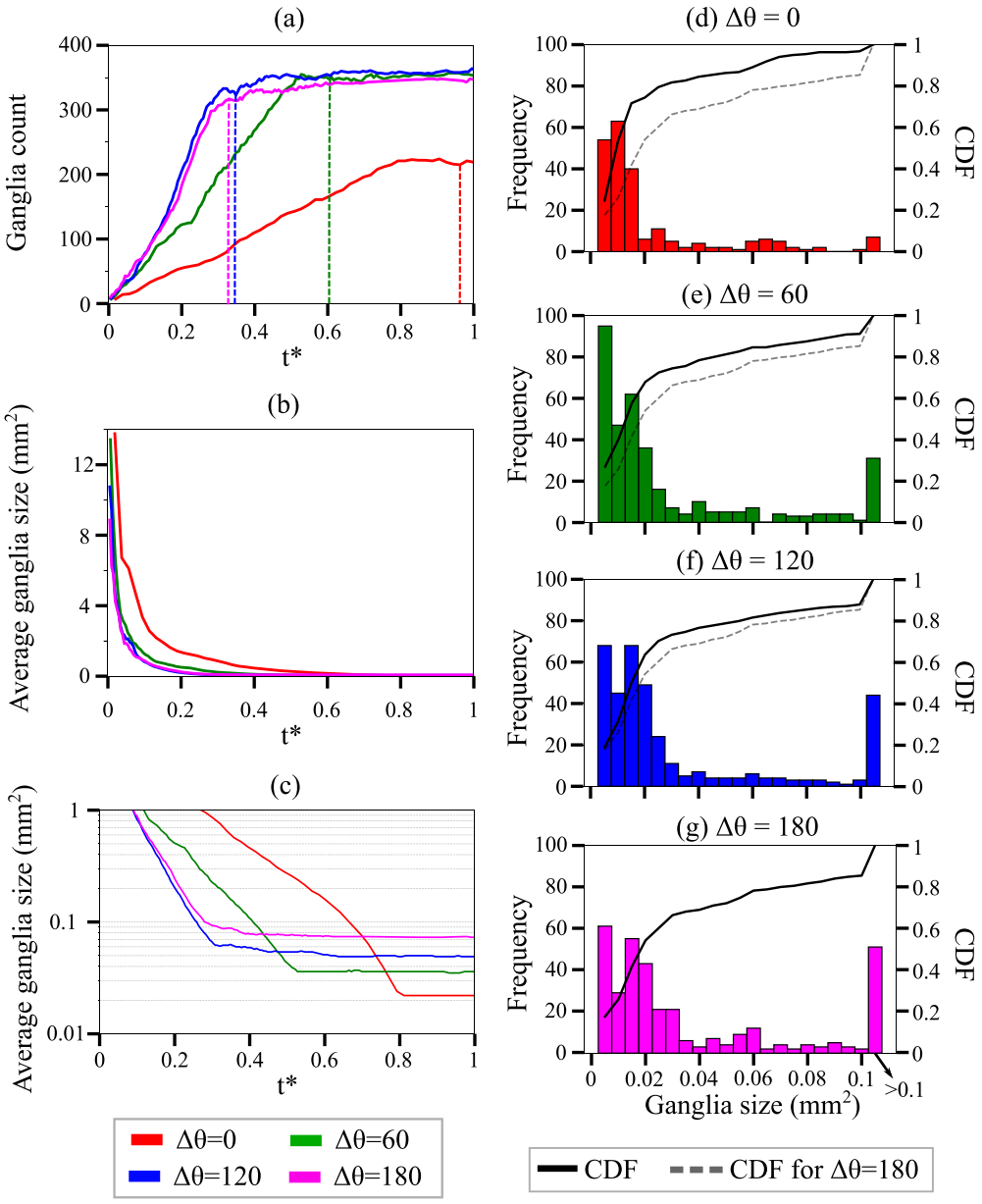

Fig. 8. Ganglia dynamics for the investigated $\Delta\theta$. (a) shows the evolution of ganglia count over time. The time has been normalized as $t^* = \frac{t}{t_{SS}}$ where t is the physical time and t_{SS} is the time taken to reach steady-state. The dashed color lines represent breakthrough time for different $\Delta\theta$. The evolution of average ganglia size in the porous medium over time is shown in (b). (c) shows the average ganglia size in (b) but on a logarithmic scale. (d) - (g) show the distribution of ganglia size at steady-state for $\Delta\theta = 0, 60, 120, 180$ respectively. The cumulative distribution function (CDF) for each $\Delta\theta$ is represented by a continuous black line. The CDF of $\Delta\theta = 180$ is shown by a dashed gray line in (d)–(f) for comparison. (For interpretation of the references to colour in this figure legend, the reader is referred to the web version of this article.)

Trapping efficiency is shown in Fig. 9b for all $\Delta\theta$. η almost grows linearly as $\Delta\theta$ increases. The trapping efficiency is as high as $\eta \approx 28\%$ for cases with the greatest variance in wettability, and as low as $\eta \approx 5\%$ for the uniform-wet case.

The sample-scale observations presented above are complemented by the pore-scale observations in the next section where we discuss the various possibilities that can result in the entrapment of the defending phase.

3.2.2. *Capillary trapping from a pore-scale perspective*

Capillary trapping is often linked to two flow mechanisms (Chatzis et al., 1983) (i). snap-off, (ii). flow bypassing. Snap-off usually happens in narrow pore constrictions and when the flows are capillary dominated (Lenormand and Zarcone, 1984; Joekar-Niasar and Hassanizadeh, 2012; Hu et al., 2017). In pore constrictions (i.e., pore throats), gradual swelling of the wetting films on grain surfaces during imbibition and the associated necking of the non-wetting phase during pore body invasion may result in snap-off and ganglia formation. Similar to the experimental observations of Hu et al. (2017) we did not observe any trapping of LV due to snap-off, as the flows considered in this study are viscous dominated. Notably, the trapping of LV for the cases investigated occur because of flow bypassing. Fig. 10 showcases the different scenarios in which HV bypasses the LV phase. For discussion, we consider flow bypassing seen in $\Delta\theta = 0, 180$. The observations hold true for the other investigated $\Delta\theta$ cases as well. Firstly, the direction of flow in combination with the local pore morphology can impact upon the trapping efficiency. When the flow encounters a solid grain, the flow is redirected towards either side of the grain (see the region of interest of Fig. 10a1) or is split owing to the balance of forces. Consequently, the LV present on the downstream side

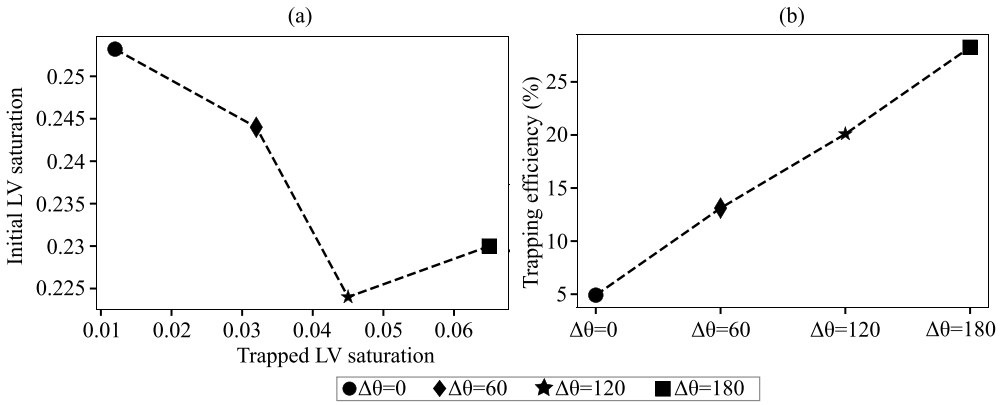

Fig. 9. Sample-scale metrics related to the capillary trapping of LV. (a) shows a comparison between the initial (start of HV flooding) and trapped LV (end of HV flooding) saturation for different $\Delta\theta$. The trapping efficiency, which is the ratio between trapped to initial LV saturation is shown in (b) for different $\Delta\theta$.

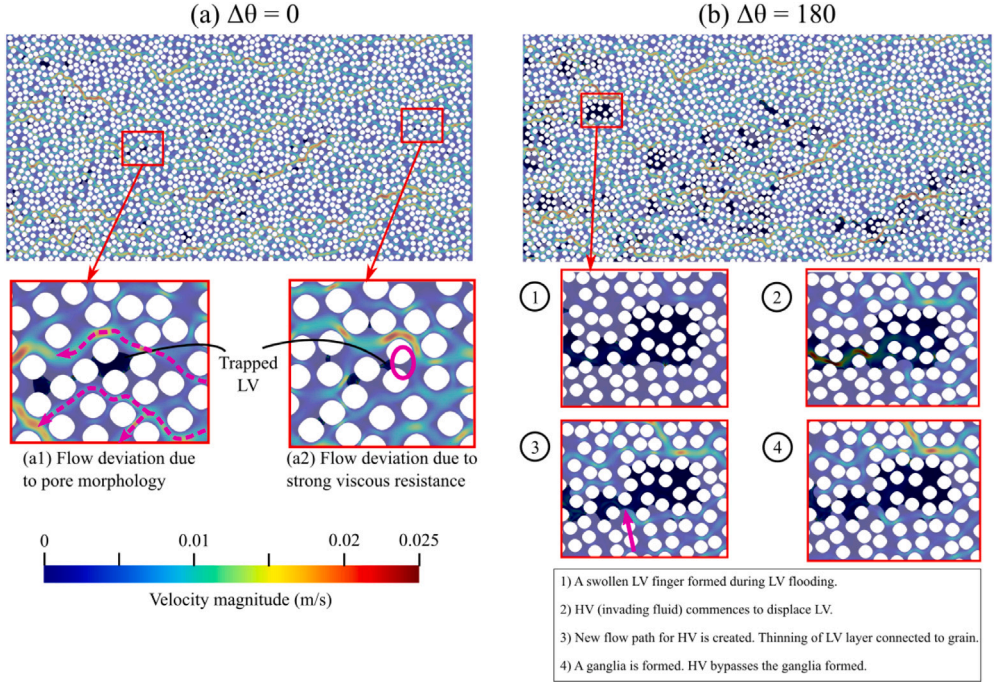

Fig. 10. A representation of the mechanisms by which LV gets trapped in the pore spaces. The flow direction is from right to left. Velocity profiles computed using DNS are shown to visualize the flow paths of the invading and defending phases. The velocity profiles are overlaid by the trapped LV ganglia shown in black for (a) $\Delta\theta = 0$ and (b) $\Delta\theta = 180$. The different ways in which LV gets trapped by flow bypassing are shown in regions of interest of (a), (b). In (a1), the dashed pink lines highlight the flow paths. In (a2), the highlighted pink ellipse shows a narrow pore space. The flow manifests to avoid invasion through this region due to viscous resistance. In (b), for the snapshot labeled 3, the pink arrow highlights the flow direction that cuts the connectivity of LV eventually resulting in the formation and entrapment of a LV ganglia. (For interpretation of the references to colour in this figure legend, the reader is referred to the web version of this article.)

of the grain potentially remains trapped. Additionally, flows through narrower pore spaces which offer greater flow resistance are often not perturbed as shown in the region of interest of Fig. 10a2. This relates to flows being focused through least resistant pathways and eventual trapping of LV in the non perturbed porous zones. For $\Delta\theta = 0$, these are two flow bypassing events that are commonly observed. Relating these observations to Fig. 8d, we can see these events promote the formation of small, isolated ganglia. Similar to $\Delta\theta = 0$, we also see a number of smaller sized ganglia trapped in the porous medium for $\Delta\theta > 0$ (Fig. 8e, f, g) as a consequence of the above mentioned flow physics.

For the mixed-wet cases, we also notice the influence of wettability on flow bypassing. In general, during HV flooding, HV prefers to invade through the LV non-wetting (i.e., HV wetting) zones. The least preference for HV invasions are through porous zones that are LV wetting, and in particular those LV wetting zones with smaller pore spaces, equating to regions with greater capillary entry pressures. In order for HV to displace LV through those zones, the pressure of HV must overcome the capillary entry pressures. Fig. 10b shows the snapshots of how a swollen LV finger in a LV wetting zone become trapped as a large ganglia during HV flooding for $\Delta\theta = 180$. Observing the flow morphology surrounding the LV finger reveals that the invading HV diverts its flow path to avoid potential incursion into the LV wetting zone. The flow manifests itself in such a manner that HV never invades the LV-wet zone and over time, the finger snaps-off resulting in the trapping of a large LV cluster in the LV wetting zone. In addition to the case presented in Fig. 10b, we also noticed that in some scenarios HV partially enters through the LV-wet zones, thereby displacing a portion of the LV defending phase, as shown in Section 5.3 of the SI. In this scenario, HV bypasses and flows around the remaining trapped ganglia. In several other cases, ganglia dynamics also assist in the entrapment of the LV phase. A mobile ganglia migrates via the LV non-wet zones and enters the LV-wet zone, eventually ends getting trapped (refer to the

video S1 and Section 5.3 of the SI). HV cannot remobilize these ganglia due to the relatively high entry pressures bounding their occupied pores, resulting in HV bypass. Consequently, we surmise that the LV-wet zones are potential hotspots for trapping substantial quantities of the defending phase.

3.3. Implications towards geological carbon dioxide sequestration

Results of this study as presented in Fig. 9 showcase that wettability has a major impact upon the quantities of CO_2 that can be effectively trapped in a CCS reservoir. Although the above conclusion has been confirmed by other studies (example, Al-Menhali and Krevor (2016), Hu et al. (2017) and Guo et al. (2022) and corresponding references therein), to date, ambiguity still exists over the ideal wetting scenarios for trapping CO_2 in the subsurface, and the pore-scale immiscible displacement mechanics that underpin such favorable regimes. Our analysis highlights that mixed-wet reservoirs that have a combination of localized imbibition and drainage zones have a significant potential in sequestrating CO_2 through capillary trapping. Critically, the greater the range in wettability of the storage medium, the greater potential for CO_2 trapping by capillarity can be expected. Studies by Arif et al. (2019), Ali et al. (2019) and Regaieg et al. (2023) and corresponding references therein have shown that core plugs possess mixed wettability (i.e., a combination of CO_2-wet and brine-wet regions). Reviews by Iglauer (2017), Chen et al. (2023) and Khan et al. (2024) shed light upon the potential pathways and controls that lead to mixed wettability in brine-CO_2-rock systems, such as the pressure-temperature regime, pore wall aging and mineralogy. They also highlight additional factors, such as fluid-rock interactions, the role of organic content and wettability altering nanoparticles, which may contribute towards mix-wet characteristics in real geologic porous media. This field of research is actively evolving and a greater understanding over the factors that impact wettability of CCS reservoirs, as well as the magnitude and ubiquity in subsurface settings will assist in constraining the characteristic properties of target reservoirs. Given the above, it can be expected that both elevated pressure-temperature and prolonged interaction between the brine-CO_2-rock system will tend to promote mixed wettability within the target geological storage medium, and by extension, optimize capillary trapping of CO_2. More specifically, we can expect porous and permeable storage formations containing mineral assemblages (example, carbonates and phyllosilicate bearing impure and/or mineralogically immature sandstones) that are more prone to $scCO_2$ wettability alteration and mixed wettability. Particularly in the case of clastic reservoirs, classic notions of sandstone compositions which tend to correlate with high quality reservoirs (i.e., clean, mineralogically mature sandstones) may not be optimal in the context of CO_2 trapping.

The results presented in Figs. 5, 7 indicate that the underlying wettability distribution controls fluid displacement morphology during flooding, being consistent with the observations of Bakhshian and Hosseini (2019) and Jahanbakhsh et al. (2021). During CO_2 flooding at relatively high injection rates (i.e., high Ca corresponding to viscous dominated flows), CO_2 always invades the porous domain in the form of viscous fingers. However, the morphological features of the developed instabilities, such as the finger length and width are controlled by the wettability in tandem with pore geometry (i.e., pore size, shape and connectivity). These flow morphological features impact the interfacial area of CO_2 in contact with brine that can initiate solubility trapping and prolonged exposure with mineral substrates can initiate mineral trapping over substantial periods of time (Iglauer et al., 2012; Bakhshian and Hosseini, 2019). If CO_2 is invading a brine-wet/ intermediate-wet porous medium, the developed fingers are generally thin and long as seen in Fig. 4. This is because, CO_2 occupies the pore spaces as random and unstable bursts. In addition, spreading of CO_2 on a brine/ intermediate-wet surface is limited (see Fig. 6, $\Delta\theta = 0$). In a mixed-wet porous medium, CO_2 preferentially flows through the CO_2-wet zones. Pore spaces having stronger affinity towards CO_2, have the greatest probability of complete pore invasion by the invading CO_2. In the CO_2-wet pore spaces, the invading fluid may enter as a burst. Over time, the front keeps spreading over grain surfaces and multiple menisci merge together initiating cooperative pore filling events. This results in a more compact/ swollen like finger structures for the CO_2 (see Fig. 6, $\Delta\theta > 0$). If a CO_2 finger propagates through the brine-wet region and there exists some CO_2 in surrounding CO_2-wet regions, there is a high likelihood that the finger retract, contributing to cooperative pore filling in the CO_2-wet regions (see Fig. 6 for $\Delta\theta = 180$). It is important to realize that not all CO_2-wet pore spaces in the reservoirs will be imbibed by CO_2. Most of the CO_2-wet pore spaces in the region of the propagating front have a greater likelihood to be occupied by CO_2, whereas, CO_2-wet regions far away from the CO_2 invading front will likely remain occupied by brine. CO_2 invading brine-wet regions is perturbed by their wettability state, though as above, this is highly dependant upon the path taken by the invading front. Most often, CO_2 entering the brine-wet regions ends up as the tip of a finger which cessates, halting further propagation through the brine-wet zones.

Considering a mono-wet system subjected to viscous dominated brine flooding at intermediate-wet conditions, the results related to capillary trapping of CO_2 were not promising. Only a small quantity of CO_2 remains trapped in the pore spaces and has a trapping efficiency as low as 5%. However, upon considering a range in the wettability, the trapping efficiency is seen to steadily increase to as high as 28% when there are a combination of strong brine-wet and strong CO_2-wet regions in the porous medium. Intriguingly from Fig. 9a, we see a trend in which the initial CO_2 saturation keeps reducing whereas, the trapped CO_2 saturation keeps increasing as the wettability range keeps increasing. For the mixed-wet cases investigated in this study, most of the CO_2 trapping occurs in the CO_2-wet regions coherent with the observations made by Bakhshian and Hosseini (2019) who studied CO_2 trapping in a fractional-wet porous medium and by Herring et al. (2021) who noticed through experiments, an increase in the CO_2 trapping efficiency due to the existence of patchy mixed-wet regions. As brine finds it difficult to invade through strong CO_2-wet porous zones, we observe larger sized ganglia getting trapped as the wettability range increases. This observation highlights the significance of the flow dynamics (i.e., finger retraction in brine-wet zones contributing to the cooperative pore filling in CO_2-wet zones) that occur during CO_2 flooding. In fact, these flow dynamics potentially contribute towards improved CO_2 trapping.

As brine bypasses the trapped CO_2, the potential to dissolve the CO_2 in contact with brine over time might present opportunities for the interface to reconfigure, which may in turn initiate mobilizations of the trapped ganglia. Even in such a scenario, the CO_2-wet zones offer relatively greater resistance against brine invasions, due to the entry capillary pressure that the invading fluid has to overcome in order to mobilize the trapped CO_2 ganglia.

The complex and dynamic invasion protocols of the fluids observed in this study also highlight the fact that mixed-wet conditions of a reservoir cannot be approximated by mono wettability. Importantly, similar values obtained for the displacement efficiency and fractal dimensions for different $\Delta\theta$ during LV flooding despite having different fingering morphologies showcases that the macroscopic metrics alone may not be sufficient to capture the pore-scale flow dynamics that eventually lead to residual trapping of the fluids. From a CO_2 sequestration perspective, the results of our study clearly highlight the fact that even though the displacement efficiency of CO_2 is approximately similar for various mixed-wet systems, the residual trapping is strongly a function of the local subsurface wettability heterogeneity. To accurately capture the subsurface flow physics in complex engineering applications such as CCS, it is imperative to consider the subsurface wettability distribution. Studies by Akai et al. (2019), Guo et al. (2022) and Regaieg et al. (2023) have shown that the mentioned oversimplification may result

in considerable differences in the behavioral patterns of reservoir-scale parameters such as capillary pressure and relative permeability. It is also well known that these reservoir-scale parameters control the overall predictability of CCS operations over spatio-temporal scales of interest.

The explicit nature of flow dynamics presented in this study using high fidelity DNS comes at the expense of considerable computational cost. Pore network models (PNMs): a subset of computationally efficient tools, have also been used to study the capillary trapping of CO_2 in porous media (Hefny et al., 2020). However, the dynamic flow phenomena observed within this study, including finger retraction leading to cooperative pore filling, viscous fingering invading pores of different sizes, and flow bypassing resulting in trapping of the defending phase are not explicitly captured by conventional PNMs. Conventional PNMs are rule-based with protocols which describe the nature of flows, including piston-type displacement, snap-off, and cooperative pore filling (Øren et al., 2019; Hefny et al., 2020). While our study does not explicitly propose any model for PNM that integrates the findings, we believe that it lays the foundation towards the inclusion of dynamic pore filling behavior within such abstracted models. In this regard, several considerations for the advancement of PNM in the light of this study's findings are: (i). To account for the mixed-wettability: instead of using mono-wet systems for realizing the fluid displacements in the pore network, it can be beneficial to account for mixed wettability. A setup if possible, as presented in Regaieg et al. (2023) where the authors use wettability information extracted from micro-CT scans for their pore network to have more reliable PNM simulations is suggested, (ii). Displacement rules: while a direct integration of the detailed DNS flow fields into a PNM is not feasible, the observed effects – such as spatially heterogeneous wettability influence on ganglia trapping and mobilization – can be translated into modified capillary entry pressures and invasion rules. These findings can potentially provide a basis for extending traditional PNMs to incorporate more realistic, wettability-aware displacement dynamics, and, (iii). Validating PNMs: based on the presented DNS results, metrics such as ganglia sizes and their distributions, fluids morphological displacement patterns that are observed under different investigated mixed-wet scenarios can be used for validating the accuracy of currently available PNMs.

Finally, it has recently been demonstrated that deep learning surrogate models can act as powerful tools towards the prediction of complex pore-scale displacement patterns in porous media, overcoming the computational limitations of DNS whilst capturing the flow morphological complexity (Wang et al., 2021; Yang et al., 2024). For example, Yaqoob et al. (2025) developed FluidNet-Lite, a lightweight CNN (convolutional neural network) that reformulates the DNS predicted two-phase flow breakthrough patterns modeled in heterogeneous porous media as a pixel-wise classification task rather than a generative framework. By embedding M, θ directly into the network, they achieved accurate, scalable predictions of breakthrough patterns in complex pore geometries, enabling faster and more reliable pore-scale flow predictions. Whilst the training data set for the above study considered multiple mono-wet scenarios, incorporating mixed wettability states and accounting for the induced dynamic flow phenomena observed herein, into the training sets of such surrogate models is critical for advancing their utility for flow pattern prediction in geologically realistic porous media with spatially complex distributions of wetting properties.

4. Conclusion

Direct numerical simulations are used to investigate viscous-dominated two-phase fluid displacement in a high-porosity, 2D porous medium under multiple realizations of mixed wettability. For all investigated cases, the sample-scale average contact angle is maintained at 90°, representing neutral-wet conditions. Mixed-wet scenarios are constructed by assigning a combination of wetting, neutral, and non-wetting sub-domains within the porous medium. The standard deviation of the contact angle is varied across the cases to exclusively assess the sensitivity of wettability heterogeneity on the fluid dynamics in a mixed-wet porous media.

During viscous fingering (low viscous fluid displacing high viscous fluid), the wettability range influences the pore-scale flow mechanisms which consequently impact the morphological characteristics of the fingering instabilities. While fingers propagate in the form of unstable bursts in the non-wet zones, cooperative pore filling is observed in the wetting zones. In particular, when the range of the wettability is greater, the developed fingers can retract and assist in cooperative pore filling. Interestingly, even after observing differences in the fingering patterns for different mixed-wet cases, the invasion morphological metrics such as displacement efficiency and fractal dimension are largely comparable among the investigated cases, indicating that the macroscopic metrics alone may not be sufficient to capture the observed pore-scale flow dynamics.

Injecting a viscous fluid into a porous medium co-occupied by fluids with different viscosity resulted in different capillary trapping patterns for the investigated mixed-wet cases. The differences in wettability dispersion for the studied mixed-wet cases play an important role in governing the ganglia mobilization and trapping dynamics, which involve coalescence and fragmentation of existing ganglia. These events influence ganglia size and trapping localization within the porous media. Specifically, as the range of the wettability increases, the average ganglia size and trapping efficiency increases commensurately. The trapping of the defending phase studied herein occurs predominantly due to flow bypassing and in those pore spaces that are wetting to the defending phase.

The results presented in this work showcase the complex nature of two phase fluid displacement occurring in mixed-wet porous media, and their implications towards practical phenomena, such as sequestrating CO_2 in mixed-wet reservoirs. Exploring a wider range of capillary numbers — particularly lower values could offer insight into flow rate dependent capillary trapping. Due to computational limitations, this was not feasible with the current setup but could be addressed in future work using a smaller porous domain. Further to this, insights from this study can be a valuable resource to develop/validate pore network models for mixed-wet systems and for training deep learning surrogate models that can predict the flow paths and capillary retention of fluids with lower computational overhead than direct numerical simulation.

CRediT authorship contribution statement

Saideep Pavuluri: Conceptualization, Data curation, Formal analysis, Investigation, Methodology, Simulations, Writing – original draft & revision. **Thomas Daniel Seers:** Writing – original draft, review, editing & revision, Formal analysis. **Nima Shokri:** Writing – review & editing, Formal analysis. **Nayef Alyafei:** Writing – review & editing, Formal analysis. **Harris Sajjad Rabbani:** Conceptualization, Data curation, Formal analysis, Funding acquisition, Investigation, Methodology, Supervision, Writing – original draft & revision.

Declaration of competing interest

The authors declare that they have no known competing financial interests or personal relationships that could have appeared to influence the work reported in this paper.

Acknowledgments

The authors would like to acknowledge Qatar Research Development and Innovation (QRDI) Council for providing financial support for this research (ARG01-0430-230039). Open Access funding is provided by the Qatar National Library (QNL).

Appendix A. Supplementary data

A supporting document with additional information referred to in the manuscript is provided. The OpenFOAM® simulation, pre-processing and post-processing files can be obtained from the authors upon request.

Supplementary material related to this article can be found online at https://doi.org/10.1016/j.ijmultiphaseflow.2025.105307.

Data availability

Data will be made available on request.

References

Akai, T., Alhammadi, A.M., Blunt, M.J., Bijeljic, B., 2019. Modeling oil recovery in mixed-wet rocks: pore-scale comparison between experiment and simulation. Transp. Porous Media 127, 393–414.

Al-Khdheeawi, E.A., Vialle, S., Barifcani, A., Sarmadivaleh, M., Iglauer, S., 2017. Impact of reservoir wettability and heterogeneity on CO2-plume migration and trapping capacity. Int. J. Greenh. Gas Control. 58, 142–158.

Al-Menhali, A.S., Krevor, S., 2016. Capillary trapping of CO2 in oil reservoirs: Observations in a mixed-wet carbonate rock. Environ. Sci. Technol. 50 (5), 2727–2734.

Al-Yaseri, A.Z., Lebedev, M., Barifcani, A., Iglauer, S., 2016. Receding and advancing (CO2+ brine+ quartz) contact angles as a function of pressure, temperature, surface roughness, salt type and salinity. J. Chem. Thermodyn. 93, 416–423.

Albadawi, A., Donoghue, D., Robinson, A., Murray, D., Delauré, Y., 2013. Influence of surface tension implementation in volume of fluid and coupled volume of fluid with level set methods for bubble growth and detachment. Int. J. Multiph. Flow 53, 11–28.

Alhammadi, A.M., AlRatrout, A., Singh, K., Bijeljic, B., Blunt, M.J., 2017. In situ characterization of mixed-wettability in a reservoir rock at subsurface conditions. Sci. Rep. 7 (1), 10753.

Ali, M., Arif, M., Sahito, M.F., Al-Anssari, S., Keshavarz, A., Barifcani, A., Stalker, L., Sarmadivaleh, M., Iglauer, S., 2019. CO2-wettability of sandstones exposed to traces of organic acids: Implications for CO2 geo-storage. Int. J. Greenh. Gas Control. 83, 61–68.

Amooie, A., Gong, Y., Sedghi, M., McCaskill, B., Piri, M., 2024. A pore-network modeling perspective on the dynamics of residual trapping in geological carbon storage. Int. J. Greenh. Gas Control. 136, 104200.

Anderson, W.G., 1986. Wettability literature survey-part 1: rock/oil/brine interactions and the effects of core handling on wettability. J. Pet. Technol. 38 (10), 1125–1144.

Arif, M., Abu-Khamsin, S.A., Iglauer, S., 2019. Wettability of rock/CO2/brine and rock/oil/CO2-enriched-brine systems: Critical parametric analysis and future outlook. Adv. Colloid Interface Sci. 268, 91–113.

Arif, M., Al-Yaseri, A.Z., Barifcani, A., Lebedev, M., Iglauer, S., 2016. Impact of pressure and temperature on CO2–brine–mica contact angles and CO2–brine interfacial tension: Implications for carbon geo-sequestration. J. Colloid Interface Sci. 462, 208–215.

Arif, M., Lebedev, M., Barifcani, A., Iglauer, S., 2017a. CO2 storage in carbonates: Wettability of calcite. Int. J. Greenh. Gas Control. 62, 113–121.

Arif, M., Lebedev, M., Barifcani, A., Iglauer, S., 2017b. Influence of shale-total organic content on CO2 geo-storage potential. Geophys. Res. Lett. 44 (17), 8769–8775.

Aziz, R., Joekar-Niasar, V., Martínez-Ferrer, P.J., Godinez-Brizuela, O.E., Theodoropoulos, C., Mahani, H., 2019. Novel insights into pore-scale dynamics of wettability alteration during low salinity waterflooding. Sci. Rep. 9 (1), 9257.

Bakhshian, S., Hosseini, S.A., 2019. Pore–scale analysis of supercritical CO2–brine immiscible displacement under fractional–wettability conditions. Adv. Water Resour. 126, 96–107.

Bakhshian, S., Rabbani, H.S., Hosseini, S.A., Shokri, N., 2020. New insights into complex interactions between heterogeneity and wettability influencing two-phase flow in porous media. Geophys. Res. Lett. 47 (14), e2020GL088187.

Bakhshian, S., Rabbani, H.S., Shokri, N., 2021. Physics-driven investigation of wettability effects on two-phase flow in natural porous media: recent advances, new insights, and future perspectives. Transp. Porous Media 140 (1), 85–106.

Blake, T., De Coninck, J., 2002. The influence of solid–liquid interactions on dynamic wetting. Adv. Colloid Interface Sci. 96 (1–3), 21–36.

Brackbill, J.U., Kothe, D.B., Zemach, C., 1992. A continuum method for modeling surface tension. J. Comput. Phys. 100 (2), 335–354.

Buckley, J., Liu, Y., Monsterleet, S., 1998. Mechanisms of wetting alteration by crude oils. SPE J. 3 (01), 54–61.

Chalbaud, C., Robin, M., Lombard, J., Martin, F., Egermann, P., Bertin, H., 2009. Interfacial tension measurements and wettability evaluation for geological CO2 storage. Adv. Water Resour. 32 (1), 98–109.

Chatzis, I., Morrow, N.R., Lim, H.T., 1983. Magnitude and detailed structure of residual oil saturation. Soc. Pet. Eng. J. 23 (02), 311–326.

Chaudhary, K., Bayani Cardenas, M., Wolfe, W.W., Maisano, J.A., Ketcham, R.A., Bennett, P.C., 2013. Pore-scale trapping of supercritical CO2 and the role of grain wettability and shape. Geophys. Res. Lett. 40 (15), 3878–3882.

Chen, Y., Saeedi, A., Xie, Q., 2023. Interfacial interactions of CO2-brine-rock system in saline aquifers for CO2 geological storage: A critical review. Int. J. Coal Geol. 274, 104272.

Chiquet, P., Daridon, J.-L., Broseta, D., Thibeau, S., 2007. CO2/water interfacial tensions under pressure and temperature conditions of CO2 geological storage. Energy Convers. Manage. 48 (3), 736–744.

Courant, R., Friedrichs, K., Lewy, H., 1928. Über die partiellen differenzengleichungen der mathematischen physik. Math. Ann. 100 (1), 32–74.

Deshpande, S.S., Anumolu, L., Trujillo, M.F., 2012. Evaluating the performance of the two-phase flow solver interfoam. Comput. Sci. Discov. 5 (1), 014016.

El-Maghraby, R.M., Blunt, M.J., 2013. Residual CO2 trapping in Indiana limestone. Environ. Sci. Technol. 47 (1), 227–233.

Farokhpoor, R., Bjørkvik, B.J., Lindeberg, E., Torsæter, O., 2013. Wettability behaviour of CO2 at storage conditions. Int. J. Greenh. Gas Control. 12, 18–25.

Fauziah, C.A., Al-Khdheeawi, E.A., Iglauer, S., Barifcani, A., 2020. Effect of clay minerals heterogeneity on wettability measurements: implications for CO2 storage. In: Offshore Technology Conference Asia. OTC, D012S001R101.

Feder, J., 1988. Fractals. Plenum Press, New York.

Fernø, M., Haugen, M., Eikehaug, K., Folkvord, O., Benali, B., Both, J.W., Storvik, E., Nixon, C.W., Gawthrope, R.L., Nordbotten, J.M., 2024. Room-scale CO2 injections in a physical reservoir model with faults. Transp. Porous Media 151 (5), 913–937.

Ferrari, A., Jimenez-Martinez, J., Borgne, T.L., Méheust, Y., Lunati, I., 2015. Challenges in modeling unstable two-phase flow experiments in porous micromodels. Water Resour. Res. 51 (3), 1381–1400.

Ferrari, A., Lunati, I., 2013. Direct numerical simulations of interface dynamics to link capillary pressure and total surface energy. Adv. Water Resour. 57, 19–31.

Flemisch, B., Nordbotten, J.M., Fernø, M., Juanes, R., Both, J.W., Class, H., Delshad, M., Doster, F., Ennis-King, J., Franc, J., et al., 2024. The FluidFlower validation benchmark study for the storage of CO 2. Transp. Porous Media 151 (5), 865–912.

Fyhn, H., Sinha, S., Roy, S., Hansen, A., 2021. Rheology of immiscible two-phase flow in mixed wet porous media: Dynamic pore network model and capillary fiber bundle model results. Transp. Porous Media 139 (3), 491–512.

Guo, R., Dalton, L., Crandall, D., McClure, J., Wang, H., Li, Z., Chen, C., 2022. Role of heterogeneous surface wettability on dynamic immiscible displacement, capillary pressure, and relative permeability in a CO2-water-rock system. Adv. Water Resour. 165, 104226.

Harvie, D.J., Davidson, M., Rudman, M., 2006. An analysis of parasitic current generation in volume of fluid simulations. Appl. Math. Model. 30 (10), 1056–1066.

Hefny, M., Qin, C., Saar, M.O., Ebigbo, A., 2020. Synchrotron-based pore-network modeling of two-phase flow in Nubian Sandstone and implications for capillary trapping of carbon dioxide. Int. J. Greenh. Gas Control. 103, 103164.

Herring, A.L., Sheppard, A., Andersson, L., Wildenschild, D., 2016. Impact of wettability alteration on 3D nonwetting phase trapping and transport. Int. J. Greenh. Gas Control. 46, 175–186.

Herring, A., Sun, C., Armstrong, R., Li, Z., McClure, J., Saadatfar, M., 2021. Evolution of bentheimer sandstone wettability during cyclic scCO2-brine injections. Water Resour. Res. 57 (11), e2021WR030891.

Hirt, C.W., Nichols, B.D., 1981. Volume of fluid (VOF) method for the dynamics of free boundaries. J. Comput. Phys. 39 (1), 201–225.

Hoang, D.A., van Steijn, V., Portela, L.M., Kreutzer, M.T., Kleijn, C.R., 2013. Benchmark numerical simulations of segmented two-phase flows in microchannels using the Volume of Fluid method. Comput. & Fluids 86, 28–36.

Hu, R., Wan, J., Kim, Y., Tokunaga, T.K., 2017. Wettability impact on supercritical CO2 capillary trapping: Pore-scale visualization and quantification. Water Resour. Res. 53 (8), 6377–6394.

Iglauer, S., 2017. CO2–water–rock wettability: variability, influencing factors, and implications for CO2 geostorage. Acc. Chem. Res. 50 (5), 1134–1142.

Iglauer, S., Fernø, M.A., Shearing, P., Blunt, M.J., 2012. Comparison of residual oil cluster size distribution, morphology and saturation in oil-wet and water-wet sandstone. J. Colloid Interface Sci. 375 (1), 187–192.

Iglauer, S., Paluszny, A., Pentland, C.H., Blunt, M.J., 2011. Residual CO2 imaged with X-ray micro-tomography. Geophys. Res. Lett. 38 (21).

Iglauer, S., Pentland, C., Busch, A., 2015. CO2 wettability of seal and reservoir rocks and the implications for carbon geo-sequestration. Water Resour. Res. 51 (1), 729–774.

Irannezhad, A., Primkulov, B.K., Juanes, R., Zhao, B., 2023a. Characteristics of fluid–fluid displacement in model mixed-wet porous media: patterns, pressures and scalings. J. Fluid Mech. 967, A27.

Irannezhad, A., Primkulov, B.K., Juanes, R., Zhao, B., 2023b. Fluid-fluid displacement in mixed-wet porous media. Phys. Rev. Fluids 8 (1), L012301.

Issa, R.I., 1986. Solution of the implicitly discretised fluid flow equations by operator-splitting. J. Comput. Phys. 62 (1), 40–65.

Jahanbakhsh, A., Shahrokhi, O., Maroto-Valer, M.M., 2021. Understanding the role of wettability distribution on pore-filling and displacement patterns in a homogeneous structure via quasi 3D pore-scale modelling. Sci. Rep. 11 (1), 17847.

Jasak, H., 1996. Error analysis and estimation in the finite volume method with applications to fluid flows.
Jiang, X., 2011. A review of physical modelling and numerical simulation of long-term geological storage of CO2. Appl. Energy 88 (11), 3557–3566.
Joekar-Niasar, V., Hassanizadeh, S., 2012. Analysis of fundamentals of two-phase flow in porous media using dynamic pore-network models: a review. Crit. Rev. Environ. Sci. Technol. 42 (18), 1895–1976.
Jung, J.-W., Wan, J., 2012. Supercritical CO2 and ionic strength effects on wettability of silica surfaces: Equilibrium contact angle measurements. Energy Fuels 26 (9), 6053–6059.
Khan, M.J., Mahmood, S.M., Alakbari, F.S., Siddiqui, N.A., Ridha, S., Shafiq, M.U., 2024. Rock wettability and its implication for caprock integrity in CO2–brine systems: A comprehensive review. Energy Fuels.
Legland, D., Arganda-Carreras, I., Andrey, P., 2016. MorphoLibJ: integrated library and plugins for mathematical morphology with ImageJ. Bioinform. 32 (22), 3532–3534.
Lei, H., Xu, T., Jin, G., 2015. TOUGH2Biot–A simulator for coupled thermal–hydrodynamic–mechanical processes in subsurface flow systems: Application to CO2 geological storage and geothermal development. Comput. Geosci. 77, 8–19.
Lenormand, R., Touboul, E., Zarcone, C., 1988. Numerical models and experiments on immiscible displacements in porous media. J. Fluid Mech. 189, 165–187.
Lenormand, R., Zarcone, C., 1984. Role of roughness and edges during imbibition in square capillaries. In: SPE Annual Technical Conference and Exhibition. SPE, pp. SPE–13264.
Liu, F., Lu, P., Griffith, C., Hedges, S.W., Soong, Y., Hellevang, H., Zhu, C., 2012. CO2–brine–caprock interaction: Reactivity experiments on Eau Claire shale and a review of relevant literature. Int. J. Greenh. Gas Control. 7, 153–167.
Morrow, N.R., 1990. Wettability and its effect on oil recovery. J. Pet. Technol. 42 (12), 1476–1484.
Nhunduru, R.A., Jahanbakhsh, A., Shahrokhi, O., Wlodarczyk, K.L., Garcia, S., Maroto-Valer, M.M., 2022. The impact of wettability on dynamic fluid connectivity and flow transport kinetics in porous media. Water Resour. Res. 58 (6), e2021WR030729.
Okasha, T.M., Al-Saleh, S., Al-Khudair, W.S., 2007. Wettability evaluation of the unayzah reservoir in central saudi arabia. In: SPE Middle East Oil and Gas Show and Conference. SPE, pp. SPE–105118.
Øren, P., Ruspini, L.C., Saadatfar, M., Sok, R., Knackstedt, M., Herring, A., 2019. In-situ pore-scale imaging and image-based modelling of capillary trapping for geological storage of CO2. Int. J. Greenh. Gas Control. 87, 34–43.
Pak, T., Rabbani, H.S., Qaseminejad Raeini, A., Shokri, N., 2023. Effects of the pore morphology on multiphase fluid displacement in porous media–a high-resolution modeling investigation. ACS Omega 8 (4), 3889–3895.
Pan, B., Li, Y., Wang, H., Jones, F., Iglauer, S., 2018. CO2 and CH4 wettabilities of organic-rich shale. Energy Fuels 32 (2), 1914–1922.
Pavuluri, S., Holtzman, R., Kazeem, L., Mohammed, M., Seers, T.D., Rabbani, H.S., 2023. Interplay of viscosity and wettability controls fluid displacement in porous media. Phys. Rev. Fluids 8 (9), 094002.
Pavuluri, S., Maes, J., Doster, F., 2018. Spontaneous imbibition in a microchannel: Analytical solution and assessment of volume of fluid formulations. Microfluid. Nanofluidics 22, 1–18.
Pavuluri, S., Maes, J., Yang, J., Regaieg, M., Moncorgé, A., Doster, F., 2020. Towards pore network modelling of spontaneous imbibition: contact angle dependent invasion patterns and the occurrence of dynamic capillary barriers. Comput. Geosci. 24, 951–969.
Pavuluri, S., et al., 2019. Direct Numerical Simulations of Spontaneous Imbibition at the Pore-Scale: Impact of Parasitic Currents and Dynamic Capillary Barriers (PhD thesis). Heriot-Watt University.
Pentland, C.H., El-Maghraby, R., Georgiadis, A., Iglauer, S., Blunt, M.J., 2011. Immiscible displacements and capillary trapping in CO2 storage. Energy Procedia 4, 4969–4976.
Purswani, P., Johns, R.T., Karpyn, Z.T., 2024. Impact of wettability on capillary phase trapping using pore-network modeling. Adv. Water Resour. 184, 104606.
Rabbani, H.S., Joekar-Niasar, V., Pak, T., Shokri, N., 2017. New insights on the complex dynamics of two-phase flow in porous media under intermediate-wet conditions. Sci. Rep. 7 (1), 4584.
Rabbani, H.S., Joekar-Niasar, V., Shokri, N., 2016. Effects of intermediate wettability on entry capillary pressure in angular pores. J. Colloid Interface Sci. 473, 34–43.
Rabbani, H.S., Seers, T.D., 2019. Inertia controlled capillary pressure at the juncture between converging and uniform channels. Sci. Rep. 9 (1), 13870.
Rabbani, H.S., Zhao, B., Juanes, R., Shokri, N., 2018. Pore geometry control of apparent wetting in porous media. Sci. Rep. 8 (1), 15729.
Raeini, A.Q., Blunt, M.J., Bijeljic, B., 2012. Modelling two-phase flow in porous media at the pore scale using the volume-of-fluid method. J. Comput. Phys. 231 (17), 5653–5668.
Rahman, T., Lebedev, M., Barifcani, A., Iglauer, S., 2016. Residual trapping of supercritical CO2 in oil-wet sandstone. J. Colloid Interface Sci. 469, 63–68.
Rasmusson, K., Rasmusson, M., Tsang, Y., Benson, S., Hingerl, F., Fagerlund, F., Niemi, A., 2018. Residual trapping of carbon dioxide during geological storage—Insight gained through a pore-network modeling approach. Int. J. Greenh. Gas Control. 74, 62–78.
Regaieg, M., Nono, F., Faisal, T.F., Rivenq, R., 2023. Large-pore network simulations coupled with innovative wettability anchoring experiment to predict relative permeability of a mixed-wet rock. Transp. Porous Media 147 (2), 495–517.
Rücker, M., Berg, S., Armstrong, R., Georgiadis, A., Ott, H., Schwing, A., Neiteler, R., Brussee, N., Makurat, A., Leu, L., et al., 2015. From connected pathway flow to ganglion dynamics. Geophys. Res. Lett. 42 (10), 3888–3894.
Rusche, H., 2002. Computational Fluid Dynamics of Dispersed Two-Phase Flow at High Phase Fractions (Ph. D. thesis). University of London.
Sedghi, M., Gong, Y., McCaskill, B., Bai, S., Wang, R., Piri, M., Masalmeh, S., 2024. Pore-to-core upscaling of two-phase flow in mixed-wet porous media: Part II-a dynamic pore-network modeling approach. Transp. Porous Media 1–40.
Shams, M., Raeini, A.Q., Blunt, M.J., Bijeljic, B., 2018. A numerical model of two-phase flow at the micro-scale using the volume-of-fluid method. J. Comput. Phys. 357, 159–182.
Singh, K., Scholl, H., Brinkmann, M., Michiel, M.D., Scheel, M., Herminghaus, S., Seemann, R., 2017. The role of local instabilities in fluid invasion into permeable media. Sci. Rep. 7 (1), 444.
Trojer, M., Szulczewski, M.L., Juanes, R., 2015. Stabilizing fluid-fluid displacements in porous media through wettability alteration. Phys. Rev. Appl. 3 (5), 054008.
Tudek, J., Crandall, D., Fuchs, S., Werth, C.J., Valocchi, A.J., Chen, Y., Goodman, A., 2017. In situ contact angle measurements of liquid CO2, brine, and Mount Simon sandstone core using micro X-ray CT imaging, sessile drop, and Lattice Boltzmann modeling. J. Pet. Sci. Eng. 155, 3–10.
Valle, L., Rodríguez, R., Grima, C., Martínez, C., 2018. Effects of supercritical CO2 injection on sandstone wettability and capillary trapping. Int. J. Greenh. Gas Control. 78, 341–348.
Van Leer, B., 1974. Towards the ultimate conservative difference scheme. II. Monotonicity and conservation combined in a second-order scheme. J. Comput. Phys. 14 (4), 361–370.
Versteeg, H., Malalasekera, W., 2007. An Introduction to Computational Fluid Mechanics: The Finite Volume Method. Prentice Hall.
Wang, Y.D., Chung, T., Armstrong, R.T., Mostaghimi, P., 2021. ML-LBM: predicting and accelerating steady state flow simulation in porous media with convolutional neural networks. Transp. Porous Media 138 (1), 49–75.
Wang, S., Tokunaga, T.K., 2015. Capillary pressure–saturation relations for supercritical CO2 and brine in limestone/dolomite sands: Implications for geologic carbon sequestration in carbonate reservoirs. Environ. Sci. Technol. 49 (12), 7208–7217.
Yang, D., Gu, Y., Tontiwachwuthikul, P., 2008. Wettability determination of the reservoir brine- reservoir rock system with dissolution of CO2 at high pressures and elevated temperatures. Energy Fuels 22 (1), 504–509.
Yang, G., Xu, R., Tian, Y., Guo, S., Wu, J., Chu, X., 2024. Data-driven methods for flow and transport in porous media: A review. Int. J. Heat Mass Transfer 235, 126149.
Yaqoob, M., Ansari, M.Y., Ishaq, M., Ashraf, U., Pavuluri, S., Rabbani, A., Rabbani, H.S., Seers, T.D., 2025. FluidNet-lite: Lightweight convolutional neural network for pore-scale modeling of multiphase flow in heterogeneous porous media. Adv. Water Resour. 200, 104952.
Yekeen, N., Padmanabhan, E., Abdulelah, H., Irfan, S.A., Okunade, O.A., Khan, J.A., Negash, B.M., 2021. CO2/brine interfacial tension and rock wettability at reservoir conditions: A critical review of previous studies and case study of black shale from Malaysian formation. J. Pet. Sci. Eng. 196, 107673.
Zacharoudiou, I., Chapman, E.M., Boek, E.S., Crawshaw, J.P., 2017. Pore-filling events in single junction micro-models with corresponding lattice Boltzmann simulations. J. Fluid Mech. 824, 550–573.
Zhang, H., Al Kobaisi, M., Arif, M., 2023. Impact of wettability and injection rate on CO2 plume migration and trapping capacity: A numerical investigation. Fuel 331, 125721.
Zhang, H., Arif, M., 2024. A review of residual trapping capacity of subsurface systems for geological storage of CO2: Measurement techniques, meta-analysis of influencing factors, and future outlook. Earth-Sci. Rev. 104764.
Zhou, J., Zhang, J., Yang, J., Jin, Z., Luo, K.H., 2022. Mechanisms for kerogen wettability transition from water-wet to CO2-wet: Implications for CO2 sequestration. Chem. Eng. J. 428, 132020.